

# Mesopelagic Particle Layers in the Dynamic Hypoxic Northern Benguela Are Shaped by Zooplankton Activity

**Key Points:**

- Layers of small and large particles observed in the oxygen minimum zone of the northern Benguela are associated with deep particle fluxes
- Zooplankton activity including diel vertical migration, particle fragmentation, and egestion shape these deep particle layers
- Near-shore currents drive the temporal variability of the deep particle layers and of the associated biological processes and fluxes

**Supporting Information:**

Supporting Information may be found in the online version of this article.

**Correspondence to:**

E. Lovecchio,  
elisa.lovecchio@noc.ac.uk

**Citation:**

Lovecchio, E., Henson, S., Carvalho, F., Briggs, N., Hilder, H., Wolff, G. A., et al. (2025). Mesopelagic particle layers in the dynamic hypoxic northern Benguela are shaped by zooplankton activity. *Journal of Geophysical Research: Oceans*, 130, e2024JC021039. <https://doi.org/10.1029/2024JC021039>

Received 16 FEB 2024



Accepted 26 FEB 2025

**Author Contributions:**

**Conceptualization:** Elisa Lovecchio, Stephanie Henson, Filipa Carvalho, Nathan Briggs, Hans Hilder, George A. Wolff, Sarah L. C. Giering, Kathryn Cook, Chelsey A. Baker, Sophie Fielding

**Data curation:** Elisa Lovecchio, Filipa Carvalho, Nathan Briggs, Hans Hilder, George A. Wolff, Kathryn Cook, Sophie Fielding, Calum Preece, Mark Stinchcombe

**Formal analysis:** Elisa Lovecchio, Nathan Briggs, Hans Hilder, George A. Wolff

Elisa Lovecchio<sup>1</sup> , Stephanie Henson<sup>1</sup> , Filipa Carvalho<sup>1</sup> , Nathan Briggs<sup>1</sup> , Hans Hilder<sup>1</sup> , George A. Wolff<sup>2</sup> , Sarah L. C. Giering<sup>1</sup> , Kathryn Cook<sup>3</sup> , Chelsey A. Baker<sup>1</sup> , Sophie Fielding<sup>4</sup>, Calum Preece<sup>2</sup>, and Mark Stinchcombe<sup>1</sup>

<sup>1</sup>National Oceanography Centre, Southampton, UK, <sup>2</sup>University of Liverpool, School of Environmental Sciences, Liverpool, UK, <sup>3</sup>University of Exeter, Exeter, UK, <sup>4</sup>British Antarctic Survey, Cambridge, UK

**Abstract** Hypoxic ( $O_2 < 60 \mu\text{mol kg}^{-1}$ ) waters are found below 27% of the ocean surface and are predicted to expand in the near future; however, the organic carbon cycle in these regions is far from understood. Here we study the origin, composition, and temporal variability of mesopelagic particle layers in the hypoxic northern Benguela. We combine ship measurements, 4 months of glider data, and a high-resolution 3D coupled model. Glider data show deep particle layers between 250 and 500 m, in the hypoxic oxygen minimum zone (OMZ), often giving rise to “deep export” events. Our data point toward biological processes generating the particle layers within the OMZ itself. Between 250 and 500 m, large particulate organic matter is fresh, small particles are more refractory, and image data show a local increase in aggregates and fecal pellets. Ship data suggest that large particles and deep export events are generated both by vertically migrating organisms importing organic carbon from the near-surface to the OMZ and by mesozooplankton constantly inhabiting the OMZ and transforming the particles there. Small suspended particles accumulate above and within the OMZ. This is likely contributed to by fragmentation via zooplankton partial feeding and reduced remineralization rates. Near-shore currents drive the temporal variability in hypoxia and the associated deep particle layers, hence modulating biological activity and export events in the mesopelagic. Our results highlight how the interplay of biological and physical processes drive the carbon dynamics of widespread hypoxic OMZs and provide insight into how to improve models in these regions.

**Plain Language Summary** Water with low oxygen concentration is found below nearly 1/3 of the ocean's surface. Low oxygen concentrations in water affect marine animals and therefore impact the cycling of carbon in the ocean, which controls climate. Here we study what determines the distribution of organic carbon in the low oxygen water found at depth in the Benguela ocean region, close to the Namibian coast, using both observational data and computer simulations. Our results show that in this region organic carbon particles are more abundant in the low oxygen water (250–500 m below the surface) than in the water found immediately above it. Data indicate that zooplankton, very small animals that live in the ocean, generate these deep particle layers while they inhabit the low-oxygen waters (smaller zooplankton) or migrate to those depths during the day to escape predators (larger zooplankton). Zooplankton produce large organic carbon particles at depth by defecating. They also fragment larger particles into smaller particles that remain suspended and accumulate there for long times. At the same time, ocean currents move these deep layers of particles around. Our results reveal how biological and physical processes work together to regulate the cycling of carbon at depth in low oxygen regions.

## 1. Introduction

Oxygen minimum zones (OMZs) are ocean regions characterized by low oxygen concentrations in the mesopelagic, which are generated by a combination of inefficient ventilation and organic carbon remineralization at depth (Karstensen et al., 2008). Globally, hypoxic ( $O_2 < 60 \mu\text{mol kg}^{-1}$ ) OMZs occupy about 5% of the ocean's volume (Deutsch et al., 2011) underlying as much as 27% of the ocean surface (calculated from World Ocean Atlas 2018) and are predicted to expand in the future (Laffoley & Baxter, 2019). Hypoxic conditions affect the metabolism of marine organisms and modulate the intersection between their habitable ranges due to the highly variable threshold of tolerance to low oxygen conditions across species (Ekau et al., 2010; Vaquer-Sunyer & Duarte, 2008). As a result, oxygen gradients found at the boundary of OMZs generate a variety of habitats that result in the vertical layering of species (Maas et al., 2014), whereas temporal changes in oxygen concentrations

© 2025. The Author(s).

This is an open access article under the terms of the [Creative Commons Attribution License](https://creativecommons.org/licenses/by/4.0/), which permits use, distribution and reproduction in any medium, provided the original work is properly cited.

**Funding acquisition:** Elisa Lovecchio, Stephanie Henson, George A. Wolff, Sarah L. C. Giering, Sophie Fielding

**Investigation:** Elisa Lovecchio, Stephanie Henson, Filipa Carvalho, Nathan Briggs, George A. Wolff, Sarah L. C. Giering, Kathryn Cook, Chelsey A. Baker, Sophie Fielding, Calum Preece, Mark Stinchcombe

**Methodology:** Elisa Lovecchio, Stephanie Henson, Filipa Carvalho, Nathan Briggs

**Project administration:** Elisa Lovecchio, Stephanie Henson, George A. Wolff, Sarah L. C. Giering

**Resources:** Stephanie Henson

**Software:** Elisa Lovecchio, Filipa Carvalho, Nathan Briggs, Hans Hilder, Sophie Fielding

**Supervision:** Stephanie Henson

**Validation:** Elisa Lovecchio, Filipa Carvalho, Nathan Briggs, Hans Hilder

**Visualization:** Elisa Lovecchio, Filipa Carvalho, Nathan Briggs, Sophie Fielding

**Writing – original draft:** Elisa Lovecchio

**Writing – review & editing:**

Elisa Lovecchio, Stephanie Henson, Filipa Carvalho, Nathan Briggs, Hans Hilder, George A. Wolff, Sarah L. C. Giering, Kathryn Cook, Chelsey A. Baker, Sophie Fielding, Calum Preece

can compress or expand marine organisms' habitable zones (Köhn et al., 2022). By impacting the livelihood and metabolic functioning of marine organisms at any trophic level, OMZs shape the ocean's biogeochemical cycles, including the organic carbon cycle (Kalvelage et al., 2011; Long et al., 2021).

Knowledge of the organic carbon cycle in these regions is still scarce. In particular, particulate organic matter (POM) distributions, fluxes, and their drivers in hypoxic OMZs remain elusive. Most research so far has focused on suboxic ( $O_2 < 5 \mu\text{mol kg}^{-1}$ ,  $\sim 0.1\%$  of the ocean's volume) or even anoxic (near zero  $O_2$  concentrations) regions dominated by anaerobic processes (Deutsch et al., 2011; Keeling et al., 2010). OMZs are thought to contribute positively to carbon sequestration rates due to reduced respiration rates in extremely low oxygen conditions, leading to deeper remineralization (Cavan et al., 2017; Loescher et al., 2016). Previous studies have found that biogeochemical transformations within suboxic OMZs are largely driven by microbial communities (Cavan et al., 2017), whose biological activity, in turn, is regulated by the availability of organic carbon-rich POM (Ganesh et al., 2015; Ward et al., 2008). Low zooplankton and nekton abundances have previously been observed in suboxic OMZs, which can constitute a boundary to vertically migrating organisms (Loescher et al., 2016; Hauss et al., 2016). On the other hand, zooplankton biomass has been observed to accumulate predominantly in the thermocline and around the upper and lower oxyclines of suboxic OMZs, particularly at oxygen concentrations of about  $60 \mu\text{mol kg}^{-1}$ , that is, in hypoxic waters (Roullier et al., 2014; Wishner et al., 2013). These zooplankton populations may repackage deep suspended material into larger and denser particles, altering the sinking flux across the OMZ (Keil et al., 2016).

Suboxic OMZs are also characterized by persistent layers of deep particles, which have been observed in the north and south tropical Pacific (Garfield et al., 1983; Pak et al., 1980; Whitmire et al., 2009; Wishner et al., 1995) and the Arabian Sea (Roullier et al., 2014). These may be produced within low oxygen waters by a combination of biological activity and physical processes (Naqvi, 1994; Naqvi et al., 1993; Wishner et al., 1995; Gowing & Wishner, 1992). Recently, a persistent layer of particles has also been observed in the hypoxic OMZ of the eastern tropical North Atlantic (Rasse & Dall'Olmo, 2019), where poorly oxygenated waters attenuated small ( $< 20 \mu\text{m}$ ) POM fluxes efficiently, whereas the opposite is true for fluxes of large POM (Rasse & Dall'Olmo, 2019; Engel et al., 2017). Such a reduction of small particle flux in hypoxic waters questions the assumption that the projected expansion of OMZs will enhance carbon sequestration rates in the ocean (Rasse & Dall'Olmo, 2019; Keeling et al., 2010).

Despite the widespread occurrence of deep particle layers and their potential role in biogeochemical cycling, there is still no clear consensus on their origin, impeding advance in mechanistic understanding of OMZ biogeochemistry. In this study, we combine high-resolution in situ and model data to investigate the origin, composition and temporal variability of mesopelagic organic carbon particle layers observed in the hypoxic offshore northern Benguela. We use a combination of 4 months of glider data spanning 0–1,000 m depth (the same glider as used for Lovecchio et al., 2022), a variety of ship-based observations and the output of a high-resolution coupled physical-biogeochemical model for the Benguela Upwelling System. Based on these data, we evaluate three potential mechanisms that could contribute, possibly independently, to the formation of these layers: (M1) biological activity within the OMZ; (M2) transport of sinking particles originating from the surface of adjacent productive regions; and (M3) transport of sediment resuspended from the shelf. The results of our study highlight the complexity of the organic carbon cycle within the mesopelagic region of hypoxic OMZs and demonstrate how both physical and biological mechanisms shape the variability of deep particle concentrations in these waters.

## 2. Methods

### 2.1. Glider Data

Glider data were collected between 14 February and 19 June 2018 at  $\sim 100$  km from the coast of the northern Benguela system using a Slocum glider (Figure 1). The glider profiled to 1000m depth following a triangular path of  $\sim 12$  km per side with a vertical resolution of  $\sim 20$  cm and emerging 5–6 times per day, sampling on the upward dive. In June, the speed of the glider was reduced to maintain position in order to facilitate final calibration and recovery. The glider was fitted with a Seabird pumped CTD, an Aanderaa optode and a Seabird WetLABS ECO-triplet sensor to measure optical backscattering at 700 nm and chlorophyll fluorescence. Note that although this sensor is targeted to detect chlorophyll-a indirectly via in vivo fluorescence (excitation at 470 nm and emission at 695 nm), the ratio of in vivo fluorescence to chlorophyll concentration varied by a factor of  $\sim 2.5$  during the 6-week cruise period. We expect similar or greater variability during the 4-month glider deployment, but lack the

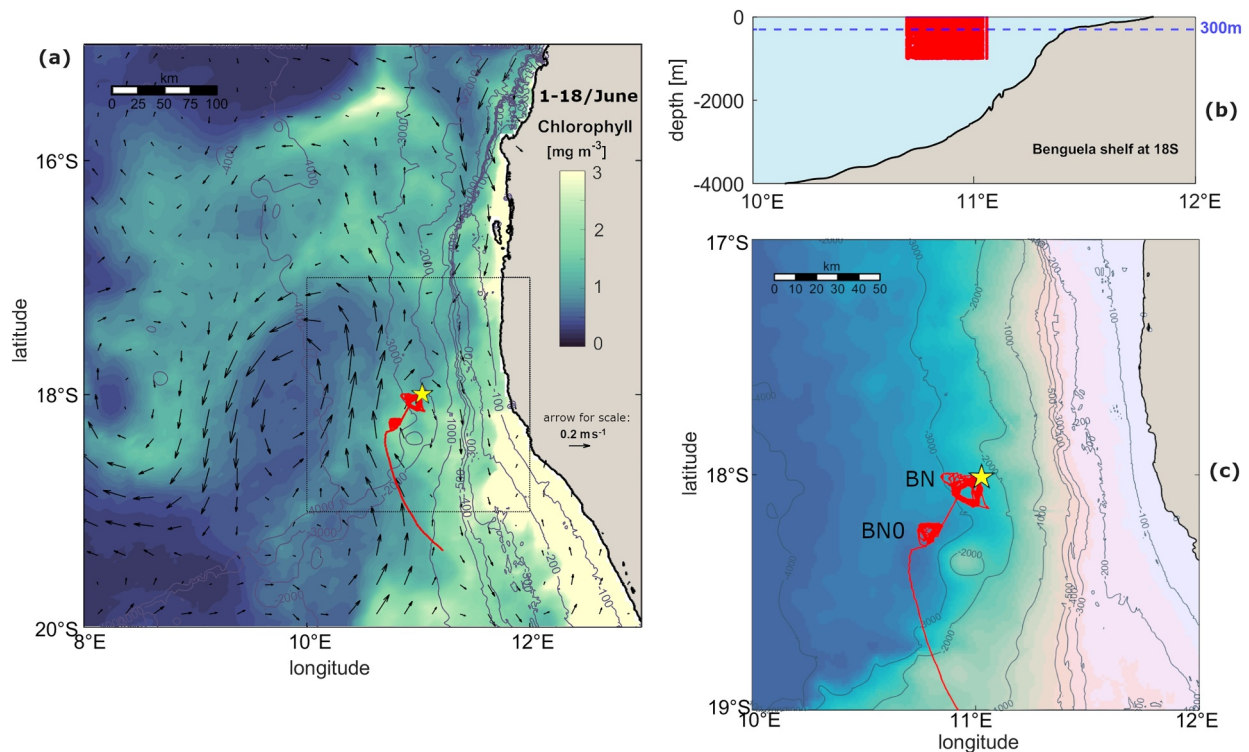


**Figure 1.** Northern Benguela region of study: (a) Satellite chlorophyll-a concentration (CMEMS GlobColour) as color shading and regional pattern of surface circulation (CMEMS DUACS), both averaged across 1–18 June 2018 (ship measurement period, overlapping the last 18 days of the glider measurement period), with depth isolines overlaid in gray, glider pathway in red and ship sampling location as a yellow star; the black dotted square shows the area of the zoom-in subplot (c). (b) Benguela shelf at 18°S with 300 m depth line highlighting the depth of the shelf break with longitude and depth range covered by the glider in red. (c) Topography as color shading with depth isolines in gray, glider pathway (red line) showing northwards transit to BNO (14–16 February) and sampling location Benguela North 0 (BNO, centered around 10.80°E 18.25°S) and Benguela North (BN, centered around 10.95°E 18.05°S), and ship sampling location at BN as a yellow star. All subplots use the same topography product (GEBCO, 2021); depth isolines are shown at 100 m intervals from 0 to 500 m and at 1,000 m intervals from 1,000 m. Additional figures showing the regional setting during the glider measurement period and additional information on the glider pathway can be found in Lovecchio et al. (2022).

data to quantify or correct it, so, although we have “calibrated” our glider fluorescence measurements in units of chlorophyll-a concentration, we still refer to this signal as “fluorescence”. Further details on the glider data collection and a full description of the temperature, salinity, and oxygen calibration of the glider data can be found in Lovecchio et al. (2022), which is based on the same survey. Conservative temperature ( $T_c$ , from here on: temperature), absolute salinity ( $S_a$ , from here on: salinity), and potential density ( $\sigma_\theta$ ) were calculated from the glider data using the TEOS-10 Gibbs Seawater Oceanographic Toolbox (McDougall & Barker, 2011). The depth of the mixed layer was calculated as the deepest depth at which  $T = T_{10m} \pm 0.8^\circ\text{C}$  (Kara et al., 2003; Lovecchio et al., 2022).

Particulate backscatter data ( $b_{bp}$ ) from the glider were partitioned into a small particle fraction ( $b_{bs}$ ) and a large particle fraction ( $b_{bl}$ ) following the methods of Henson et al. (2023), adapted from Briggs et al. (2011), using an 11-point running minimum followed by an 11-point running maximum filter (Briggs et al., 2011, 2020) to distinguish the presence of “large particles” ( $b_{bl}$ ) with equivalent spherical diameter larger than  $\sim 470 \mu\text{m}$  (Henson et al., 2023) from that of “small particles” ( $b_{bs}$ ). According to this decomposition,  $b_{bp} = b_{bl} + b_{bs}$ . By applying a running minimum followed by a running maximum filter to individual vertical  $b_{bp}$  profiles, spikes in the backscatter signal are attributed to the presence of large individual particles, whereas the residual signal (including instrument noise) is attributed to small particles. A similar analysis was applied to glider fluorescence. Note, however, that spikes in the fluorescence signal represent particles with high chlorophyll content, and do not necessarily provide an indication of their size.

In this study, we use glider temperature, salinity, density, and dissolved oxygen ( $\text{O}_2$ ) in the form of binned medians (as in Lovecchio et al. (2022)). Backscattering ( $bbp700$ ) and fluorescence data are used in the form of binned means in order not to get rid of the meaningful signal generated by larger and brighter particles, which may

appear as outliers in the full-resolution data. Each bin corresponds to an interval of 6 hr in time (usually 1–2 profiles) and 2 m in depth.

Water masses in the glider data were identified by calculating the difference between glider salinity and oxygen profiles and the February–June climatological mean profiles (WOA2023 Salinity; WOA2018 Oxygen; Boyer et al., 2018) of the water masses found north (South Atlantic Central Water, SACW) and south (Eastern South Atlantic Central Water, ESACW) of the measurement location, as in Lovecchio et al. (2022). Each bin in the glider data at time  $t$  and depth  $z$  was tagged as: “SACW” if  $\Delta S_{SACW}(t,z) = S_{glider}(t,z) - S_{SACW}(z) \geq -0.05$  and  $\Delta O_{SACW}(t,z) = O_{glider}(t,z) - O_{SACW}(z) \leq 15 \mu\text{mol kg}^{-1}$ ; “ESACW” if  $\Delta S_{ESACW}(t,z) = S_{glider}(t,z) - S_{ESACW}(z) \leq 0.05$  and  $\Delta O_{ESACW}(t,z) = O_{glider}(t,z) - O_{ESACW}(z) \geq -15 \mu\text{mol kg}^{-1}$ ; “Hypoxic-fresh” if  $O_2 < 60 \mu\text{mol kg}^{-1}$  but salinity does not satisfy the SACW salinity rule. These chosen thresholds are less than half of the mean difference between the salinity and oxygen February–June WOA mean profiles of SACW and ESACW in the depth range of interest (150–600 m). Note that no bin fulfilled both the ESACW and SACW criteria. Plots showing  $\Delta S_{SACW}$ ,  $\Delta O_{SACW}$ ,  $\Delta S_{ESACW}$ ,  $\Delta O_{ESACW}$  can be found in Figure 6 of Lovecchio et al. (2022). SACW and ESACW were also identified in the temperature-salinity diagrams as in Lovecchio et al. (2022).

## 2.2. Ship Data

Cruise DY090, undertaken as part of the COMICS program (Sanders et al., 2016), took place in May–June 2018, about three months after the glider was deployed and overlapped the glider measurement period for its last 18 days. Ship data used in the present manuscript were collected at 11.02°E, 18.01°S ~ 4.5 km distant from the glider between 01 June and 18 June (Figure 1c).

### 2.2.1. Dissolved Oxygen Data From CTD Sensor

CTD oxygen data used in this manuscript were collected using a dissolved oxygen sensor mounted on the CTD frame (SBE-43). This was calibrated against dissolved oxygen concentration bottle samples collected on 25 of the CTD casts (see also Lovecchio et al., 2022). The bottle oxygen concentration was evaluated using Winkler titration and used to correct the CTD oxygen profiles.

### 2.2.2. Organic Geochemistry of Particulate Organic Matter

Particulate material from a range of water depths was collected using stand-alone pumps (SAPs Challenger Oceanic). Up to five SAPs were used on the same deployment to collect vertical profiles through the upper mesopelagic (20–500 m). The pumps were set to operate for one or 1.5 hr, depending on the expected particle load. Two size fractions were recovered; the  $<53 \mu\text{m}$  particle fraction was collected on large (293 mm diameter), pre-combusted (400°C; 4 hr) GF/F filters (nominal pore size 0.7  $\mu\text{m}$ ). Large particles ( $>53 \mu\text{m}$ ) were collected on acid-cleaned (10% HCl) nylon mesh screens (Nitex; pore size 53  $\mu\text{m}$ ) located above the GF/F filters. Upon recovery, the Nitex screens were carefully placed on the side of a large funnel and rinsed with filtered seawater (0.6–1 L) into 1 L acid-washed (10% HCl) glass bottles. This water was then filtered using a glass rig through pre-combusted (400°C; 4 hr) 47-mm diameter GF/F filters. All GF/F filters were stored frozen ( $-80^\circ\text{C}$ ), before freeze drying prior to analysis.

POM lipids were extracted and analyzed following the method of Kiriakoulakis et al. (2004). Compounds were identified either by comparison of their mass spectra and relative retention indices with those available in the literature and/or by comparison with authentic standards. Lipid data were analyzed statistically (PAST 4.01) to assess whether there were significant differences between samples. To deal with the large differences in concentration between surface and deeper samples and to compare suspended POM and sinking POM, the quantitative data were converted to mol% of total identified lipid. Analysis of similarity (ANOSIM) tests were performed on the biomarker data sets grouped by particle size and water depth to assess whether the differences in POM composition were statistically significant. Similarity Percentages (SIMPER) tests were applied to those groups of data that were shown to be significantly dissimilar from each other by ANOSIM, to identify the compound classes contributing the most to the variability between groups.

Following SIMPER, principal component analysis (PCA) was used on grouped biomarker compound classes to visualize the variability between the groups and highlight which lipid classes contributed to it. POM lipids are structurally diverse and have some source specificity to phytoplankton (e.g., eicosapentaenoic acid, 20:5( $n - 3$ ),

diatoms; Volkman, 2006), zooplankton (e.g., 20:1( $n - 9$ ) and 22:1( $n - 11$ ) fatty acids and equivalent monounsaturated alcohols, copepods; Dalsgaard et al., 2003; Duineveld et al., 2012), and bacteria (branched and odd carbon numbered  $n$ -alkanoic acids; Wakeham, 1995). Furthermore, their structural diversity impacts their turnover, for example, polyunsaturated fatty acids (PUFAs) and monounsaturated fatty acids (MUFAs) are significantly more labile than their saturated fatty acid counterparts (e.g., de Froe et al., 2022 and references therein).

### 2.2.3. Particle Camera Images

In-water particle images were collected using a “P-CAM” underwater camera system mounted on a profiling frame. The P-CAM system consists of a Canon EOS 6D digital SLR equipped with a 50 mm macro lens and a Canon Speedlite 600EX RT flash gun, each enclosed in a pressure housing. The camera was aimed at a black plate, and the flash was mounted perpendicularly. The height, width, and depth of the illuminated, in-focus field of view for each image was  $157 \times 101 \times 135$  mm, respectively (2.14 L). The pixel width varied from 33 to 61  $\mu\text{m}$  from front to back of the depth of field. In order to investigate the composition of the large-particle layers seen by the glider backscattering, we analyzed images from a single profile to 500 m depth in the early morning ( $\sim 1$ – $2$  a. m.) of 09 June to 500 m depth. For each image we calculated mean image brightness, which, due to the  $90^\circ$  orientation between camera and flash, is a measure of particulate scattering. Brightness was normalized for variations in flash intensity using median intensity from a piece of tape visible in each image on a portion of the back plate. Image brightness was then partitioned into small- and large-particle fractions analogous to bbs and bbl measured by the gliders. Each image was divided into  $90 \times 90$  pixel ( $\sim 4.2 \times 4.2$  mm) squares, and the median brightness of each square was calculated in order to isolate the “background” brightness due to small-particle scattering from that of individual large particles. We interpret the mean of these  $90 \times 90$  pixel medians as “small-particle brightness” and the difference between total and small-particle brightness as “large-particle brightness”. We studied the P-CAM images to observe changes in the type and abundance of particles and living organisms at each depth. For each of the 96 images collected on 9 June in the depth range 300–440 m (which coincided with a plume of large particles), we manually counted the particles that could be clearly identified as zooplankton or nekton. We then calculated the average number of identified organisms per image in that depth range.

### 2.2.4. Acoustic Backscatter Data

A multi-frequency (38, 70, and 120 kHz) drop-keel mounted echosounder (Simrad EK60) collected acoustic backscattering data ( $S_v$ , dB re  $1 \text{ m}^{-1}$ ) throughout the cruise. Here we use acoustic backscatter as a proxy for zooplankton and micronekton biomass (depending on frequency). A 3 s ping rate was used, and raw data were collected to 1,500 m (with the usable range depending on frequency). The echosounder was calibrated using standard sphere techniques (Demer et al., 2015) whilst freely drifting in the survey area. Frequency specific mean values of absorption coefficient (Francois & Garrison, 1982) and sound speed (Mackenzie, 1981) were derived from CTD profiles for the typical depth ranges encompassed by each frequency. Data were processed in Echoview V10 (10.0.293.38183): sound speed and absorption values were updated, noise was cleaned (transient and intermittent noise was set to  $-999$  dB and background noise was removed, and data were either exported at full resolution (0.19 m vertical resolution, 3 s horizontal resolution) or resampled and then exported ( $S_v$ , dB re  $1 \text{ m}^{-1}$ ) in cells of 10 m vertical resolution and 10 min horizontal resolution.

Acoustic backscatter data as a function of time across a 24H period were plotted at full resolution (3 s, 0.19 m). In order to assess potential diel vertical migration (DVM) of organisms, day-night differences in acoustic backscattering strength were calculated from the day time and night time mean acoustic profiles for each day of interest using data binned to 10 min and 10 m. The differences were smoothed using a three-point running mean in order to limit noise. We used NOAA's Sunrise/Sunset Calculator (<https://gml.noaa.gov/grad/solcalc/sunrise.html>) to retrieve the time of the apparent sunrise and sunset at the time and location of the measurements. We applied a time buffer of 2 hr after sunrise and before sunset and 1 hr before sunrise and after sunset to exclude the periods in which migration is most intense and only account for the hours of the day and night when the patterns identified in the acoustic data occupy a range of depths that is mostly constant.

### 2.2.5. Zooplankton Biomass Data

A Hydrobios Mammoth Net (1 m<sup>2</sup> opening, 300 μm mesh, hauled at 0.2 m s<sup>-1</sup>) was deployed vertically to sample mesozooplankton from 750 m to the surface in 9 discrete depth intervals: 750–625 m, 625–500 m, 500–375 m, 375–250 m, 250–188 m, 188–125 m, 125–162 m, 62–31 m, and 31–5 m. Mammoth deployments were repeated day and night. The volume of water filtered by the Mammoth nets was calculated using the net dimensions and depth of water sampled assuming 100% efficiency (Ward et al., 2012). Samples were preserved in 4% borax buffered formaldehyde for biomass analysis using a FlowCam Macro (Yokogawa Fluid Imaging Technologies). The preserved samples were sub-sampled using a Folsom splitter where necessary, such that a minimum of 2000 particles were counted. Images were collected using a 5-mm flow cell, a flow rate of 700 mL min<sup>-1</sup> and an auto-image mode rate of 10 frames per second. Carbon biomass was calculated for each particle using the area (FlowCam's Area (ABD) algorithm, mm<sup>2</sup>) to dry mass (mg) regression for general mesozooplankton from Lehette and Hernández-León (2009) and a standard dry mass to carbon conversion factor of 0.45 (Giering et al., 2019).

### 2.3. Coupled Model

We used 3D regional model simulations developed using the UCLA-ETH version of the Regional Oceanic Modeling System ROMS (Shchepetkin & McWilliams, 2005) coupled at run-time to the biological elemental cycling model BEC (Moore et al., 2013). The physical model ROMS resolves the 3D hydrostatic primitive equations of flow. ROMS's prognostic variables are surface elevation, potential temperature, salinity, barotropic and baroclinic horizontal velocities. Vertical mixing is calculated using a nonlocal K-Profile parameterization (Large et al., 1994). ROMS integrates the equations on a discretized grid and terrain-following vertical coordinates (sigma levels).

We use here the version of the BEC model (Moore et al., 2004) further developed by Frischknecht et al. (2018). The model resolves the cycling of carbon, oxygen, nutrients, three phytoplankton functional types (small phytoplankton, diatoms, and diazotrophs) and one zooplankton type. Modeled organic carbon in BEC can be either in dissolved form, as dissolved organic carbon (DOC), or in particulate form (POC), the latter being either associated with living organisms (phytoplankton and zooplankton) or non-living particulate organic carbon (detrital POC). Detrital POC is explicitly resolved by the model and is produced by phytoplankton loss terms (aggregation, mortality, sloppy grazing by zooplankton) and by zooplankton loss terms as a fixed fraction. Modeled detrital POC is either 'free' or 'quantitatively associated' to ballasting minerals; these two detrital POC classes sink respectively at constant speeds of 10 m d<sup>-1</sup> and 25 m d<sup>-1</sup> but have remineralization rates that are depth-, ballasting- and oxygen-dependent. The O<sub>2</sub> dependency is represented by a multiplying factor that decreases from 1 to a minimum of 0.3 between 40 mmol m<sup>-3</sup> and 5 mmol m<sup>-3</sup>. A small fraction of ballasted detrital POC is assumed to be refractory. The BEC model does not allow for sediment resuspension nor detrital POC fragmentation, and bacteria are not explicitly resolved. A full description of the model version used here is provided in Frischknecht et al. (2018).

Our coupled Benguela model runs on a grid spanning from -23°N to -13°N and from 3°E to 15°E, with horizontal resolution of 1/32°, corresponding to 3.2–3.4 km horizontal spacing (Figure SB1 in Supporting Information S1). Vertically, we use 42 sigma levels with surface refinement. The model is initialized at rest and integrated with a timestep of 5 min. The analysis run follows a 6-year spin-up. The analysis output is saved as 3D daily mean fields for the months of February–June 2018, which include the glider measurement period. Physical boundary conditions are derived from the daily-mean GLORYS12V1 global reanalysis model output for year 2018 at 1/12° resolution (CMEMS GLORYS data). Biogeochemical boundary conditions for oxygen and inorganic nutrients are derived from 1° × 1° World Ocean Atlas 2018 (Garcia et al., 2019), whereas dissolved organic nutrients, dissolved iron, and ammonium are derived from a global CESM-BEC simulation (Yang et al., 2017). Boundary conditions for dissolved inorganic carbon and alkalinity are derived from 1° × 1° GLODAPv2 (Lausvet et al., 2016); chlorophyll, biomass and associated organic carbon pools are estimated from surface products (SeaWiFS NASA-OBPG, 2014; Morel & Berthon, 1989). Atmospheric forcing is derived from ERA5 reanalysis for 2018 (Hersbach et al., 2023), used in the form of daily-means; radiative forcing is further corrected using the Drakkar Forcing Set (DFS5.2) (Dussin et al., 2016) following Lovecchio et al., 2017. Atmospheric dust deposition is derived from Mahowald et al., 2005; atmospheric pCO<sub>2</sub> is derived from Landschützer et al. (2013).

Figures and a detailed model evaluation are provided in Supplement B and C. To summarize, the coupled model reliably represents the key properties of interest for this study. In particular, the model successfully replicates the latitudinal gradients in physical and biogeochemical properties characterizing the transition from the Angola to the Benguela region, the location of the Angola-Benguela front, the pattern of currents and the cross-shore gradient in production due to upwelling (Figures SB2–SB5 in Supporting Information S1). The model also successfully reproduces some prominent mesoscale features observed in the satellite data, such as the energetic cross-front anticyclone observed in May (Figure SA7 in Supporting Information S1). Some significant discrepancies between model and data are found at 50 m depth, due to a vertical shift in the thermocline/halocline—a difference that may be contributed to by residual temporal variability associated with the presence of mesoscale features in the 6-month mean model analysis output (Figures SB6 in Supporting Information S1). The spatial pattern of oxygen is remarkably close to that of climatological means at the surface and at depth, with differences arising from the presence of mesoscale features in the model run; the oxygen minimum zone, however, is shallower and less intense than observed in data, likely due to the simplified representation of sediments, remineralization and mesopelagic processes in the model (Figures SB2, SB5, and SB6 in Supporting Information S1). Our biogeochemical model does not reproduce the deep particle layers observed in the in situ data (Figure SB7 in Supporting Information S1). Although this is a model limitation, this finding provides us with useful information to exclude certain mechanisms of formation of the deep particle layers, as elaborated upon in the Results and Discussion sections.

### 3. Results

#### 3.1. Mesopelagic Particle Layers From Glider Data

Glider data show high variability in small (<470  $\mu\text{m}$ ) and large (>470  $\mu\text{m}$ ) particle optical backscattering at all depths (Figure 2). In the near surface, the highest particle concentrations are bound by the mixed layer depth (MLD) and by the depth of the  $26 \text{ kg m}^{-3}$  isopycnal. Plumes of both small and large sinking particles appear to sink from the mixed layer in early March, mid-April, and mid-May, attenuating rapidly in the upper 300 m. In the upper mesopelagic sub-monthly fluctuations in backscattering follow a similar pattern to temperature, salinity and oxygen (Figure SA1 in Supporting Information S1). In particular, recurrent small and large particle clouds span the range of 250–500 m, where we also find intermittent hypoxic conditions (Figure 2) as well as the OMZ core, where waters are hypoxic on average (~380 to 450 m, Figure 3). This points to an association between deep particle clouds and the OMZ.

Small particle concentrations have a deep secondary maximum that peaks on average across the sampling period just above the depth of the hypoxic OMZ core, at ~350 m (Figure 3). Initially, when the glider samples around BN0 in February–March, small particles show an overall higher small particle background concentration at depth. During this period the glider is collecting measurements within a patch of high-chlorophyll water reaching the study site from the nearshore upwelling region (Lovecchio et al., 2022) and glider data indicate intense export events from the near-surface ocean (e.g., in early March). Nevertheless, small particles at BN0 clearly show a deep particle maximum located on average at ~320 m (Figure 3c). From late March, when the glider starts sampling at BN, small particles decrease sharply below the MLD and show deep maxima located above and at the top of the hypoxic layer, in a range of 250–450 m. These result in a deeper mean secondary maximum found on average at 355 m (Figure 3c). During June, when ship data were collected, small particle layers are visible between 200 and 400 m and then intensify during 15–17 June between a depth of 200–300 m, which corresponds to the top of the hypoxic domain (see the June zoom-in of Figure SA2 in Supporting Information S1).

Large particle backscattering also shows deep maxima located below the most productive near-surface layer, primarily in the range of 300–500 m depth but sporadically extending upwards to 200 m depth (Figure 2b). Deep maxima of large particles are clearly visible across the whole measurement period with little difference between BN0 and BN. On average, the deep large particle maximum is centered around the hypoxic layer at ~380 m, ~30 m below the average deep maximum of small particle concentration (Figure 3). Large particles are spread around and below hypoxic domains. An exception to the co-occurrence of hypoxia and deep particle maxima (both large and small) is observed during the particularly shallow hypoxic event at the beginning of April, between 75 and 300 m. In our previous study focusing on oxygen dynamics using the same data (Lovecchio et al., 2022) we identified this shallow anomaly as a subsurface anticyclonic eddy. We comment on this anomaly and its influence on particle concentrations further in the Discussion section.

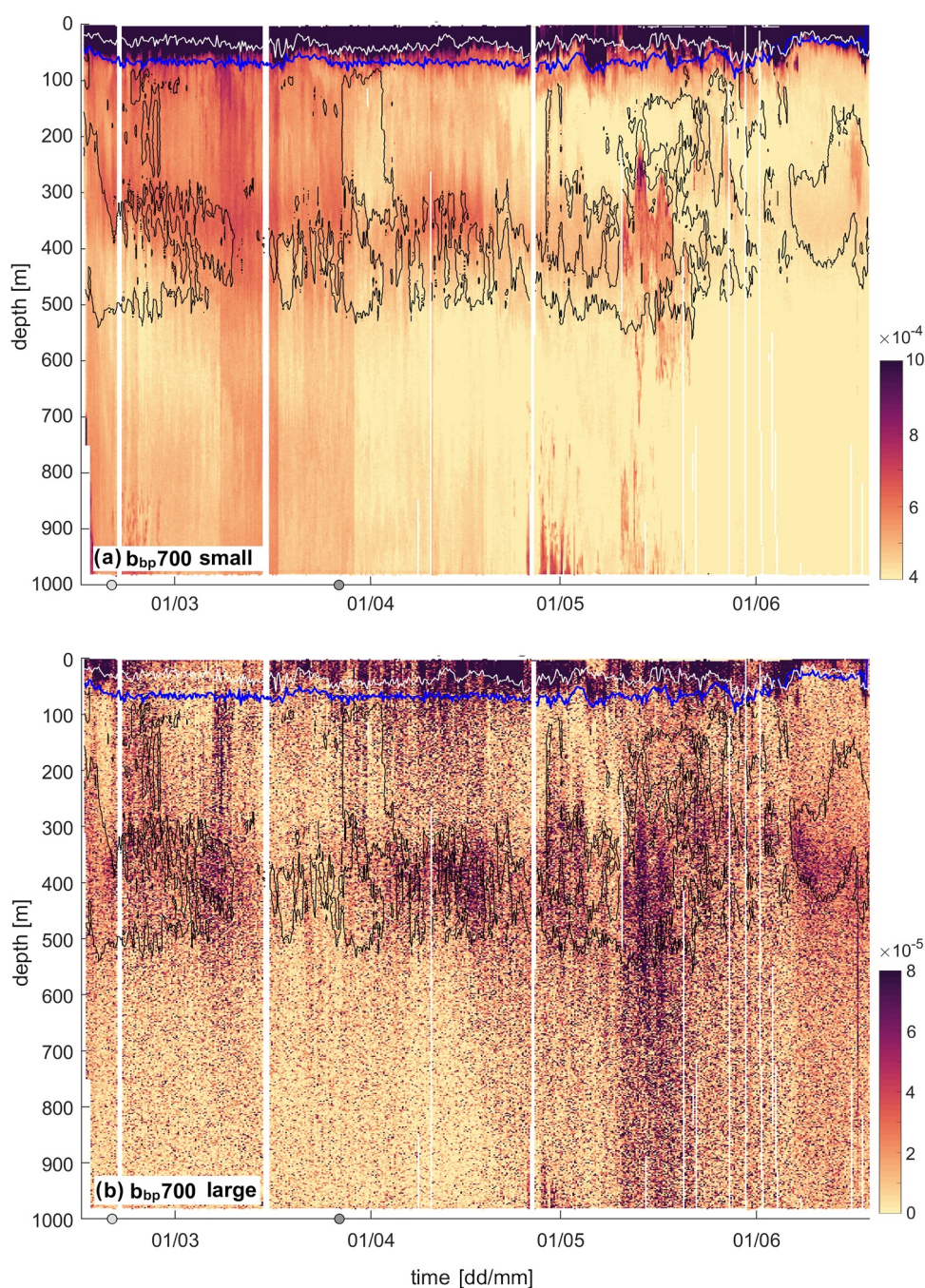


**Figure 2.** Glider optical backscattering ( $b_{bp700}$ ) with contours of hypoxia ( $O_2 = 60 \mu\text{mol kg}^{-1}$ , black line), MLD (white line) and  $26 \text{ kg m}^{-3}$  isopycnal (blue line). (a) Small ( $<470 \mu\text{m}$ ) particle backscattering; (b) Large ( $>470 \mu\text{m}$ ) particle backscattering. The day of arrival of the glider at measurement stations BN0 and BN are marked on the  $x$  axis with, respectively, a light gray circle and a dark gray circle; additional details on the glider's pathway are provided in Figure 1 and in Lovecchio et al. (2022).

Our particle distributions, particularly those of large particles, are often associated with deep-reaching plumes of particles extending downwards to at least 1,000 m (Figure 2). These particle plumes indicate sinking fluxes (similar to those used to track flux pulses by Briggs et al., 2020) that appear to originate within the OMZ and show little connection with the particle dynamics of the productive mixed layer. The observed deep flux appears to originate from within the OMZ in early March, mid to late April, early June, and most strikingly in mid-May (10–20 May), when high large particle concentrations span from  $\sim 200$  m depth to at least 1,000 m depth. During this



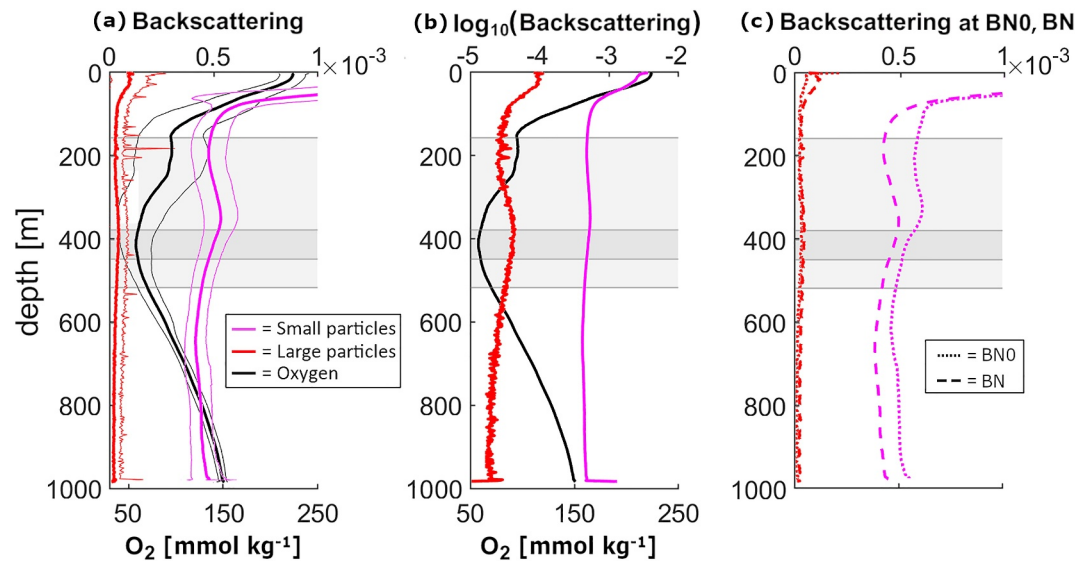


**Figure 3.** Mean profiles across the entire glider measurement period for oxygen (black line, lower  $x$ -axes) and optical backscattering ( $b_{p700}$ ) (colored lines, upper  $x$ -axes): small ( $<470\ \mu\text{m}$ ) particle backscattering (magenta line), large ( $>470\ \mu\text{m}$ ) particle backscattering (red line). (a) Mean backscattering in linear scale; note that the near-surface small particle backscattering maximum is off-scale to allow visualization of the secondary deep maximum; thinner lines mark the standard deviation around the mean for each variable. (b) Mean backscattering in  $\log_{10}$  scale; (c) Mean backscattering in linear scale calculated separately across measurement period BN0 (dotted lines) and BN (dashed lines). The gray shading in the background of both subplots marks the range of depths in which glider-derived oxygen falls below the hypoxic threshold of  $60\ \mu\text{mol kg}^{-1}$  on average (hypoxic OMZ core—dark gray, depth range: 379–449 m) or within one standard deviation from the mean (light gray, depth range: 157–517 m).

mid-May “deep-export” event, hypoxic waters between 200 and 500 m show a combined increase of both small and large particle backscattering (Figure 2), associated with a plume of chlorophyll fluorescence spikes indicating the presence of fresh organic material, that is, organic material produced relatively recently by photosynthetic organisms (Figure SA3 in Supporting Information S1). During June, large-particle layers are found at the bottom of and below hypoxic layers (between 300 and 600 m depth), with significant temporal variability in their depth (Figure SA2 in Supporting Information S1).

### 3.2. Mesopelagic Particle Properties

More insight into the nature of the deep particle layers is gained via the analysis of ship data collected in the first half of June. The analysis of camera image brightness from 9 June shows that, on this specific day, large particles concentrations are elevated in the depth range 350–430 m (Figure 4a), in agreement with the glider data (Figure 2 and June zoom-in of Figure SA2b in Supporting Information S1) and the CTD beam attenuation for the same day (Figure SA4a in Supporting Information S1). CTD oxygen data collected  $\sim 30$  min after the camera images show that a hypoxic OMZ that spans the range of  $\sim 250$  to 400 m depth (Figure SA4a in Supporting Information S1). According to camera images, both small and large particles are abundant at shallow depths (particularly at depths  $<20$  m), whereas fecal pellets are particularly abundant at 20–40 m depth (Figures 4b and 4c). Down to 300 m depth, particles are sparse and relatively small (Figures 4d and 4e). Here, individual spikes in the image brightness correspond to large sporadic objects, most notably a long aggregate (Figure 4f) and a chaetognath (Figure 4g). Between 300 and 440 m, corresponding to depths within and just below the OMZ, large particle brightness increases on average. In this range, especially below 350 m, we observe an increase in large detritus, particularly of long and thin fecal pellets and fluffy aggregates, including some bright green and possibly fresh ones (Figures 4h–4m). Some of the images ( $\sim 1$  every 3.5 images) collected between 300 and 440 m captured the presence of one, or rarely two, zooplankton (Figures 4n–4r). The great majority of the largest particles captured by the images could be clearly identified as either detritus or aggregates. We therefore conclude that the increase in large-particle brightness at these depths is not directly driven by the presence of living organisms.

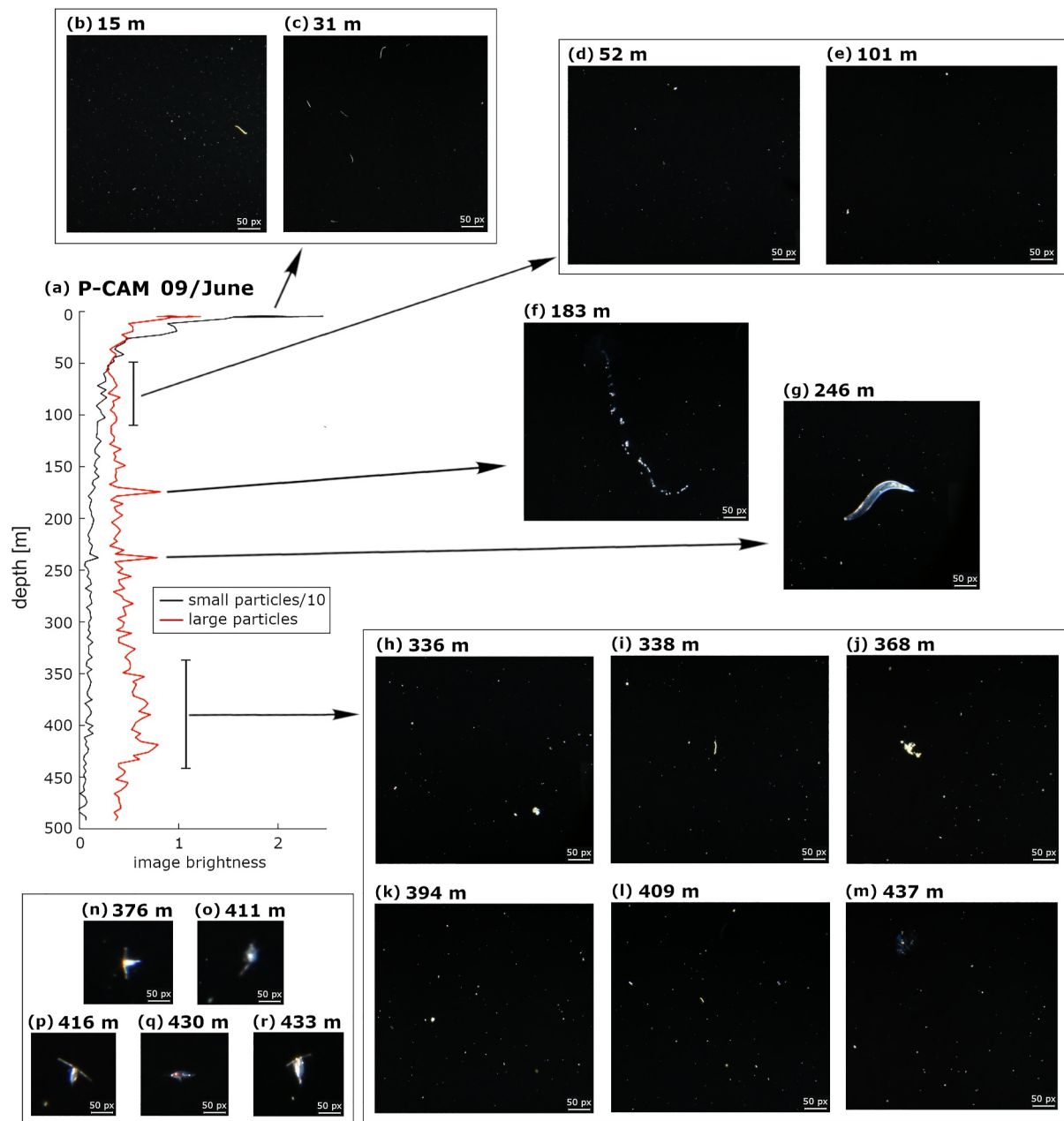


**Figure 4.** (a) Particle brightness from P-CAM images collected on 9 June from 0:59 to 01:57 (night time); (b–m) Portions of P-CAM images of the same size showing the types of particles and aggregates found at different depths; (n–r) examples of organisms identified in the images (not exhaustive of all the occurrences observed). Note that images were cropped, but not rescaled. Because of the three-dimensional nature of the camera images objects can look larger or smaller due to perspective and each image pixel corresponds to 33–61  $\mu\text{m}$ . We added a 50-pixel (50-px) bar, corresponding to 1,650–3,050  $\mu\text{m}$ , to the bottom-right corner of each image.

Lipid biomarker data of POM collected using SAPs during June (Figure 5) suggests that large POM (>53  $\mu\text{m}$ ) and small POM (<53  $\mu\text{m}$ ) particles are significantly different in composition (ANOSIM;  $p < 0.0001$ ), as visualized by principal component analysis (Figure 5a). Below 250 m, large particles are nearly always “fresh”, as confirmed by consistently higher proportions of PUFAs and MUFAs relative to saturated fatty acids (SIMPER, Saturated fatty acids, MUFAs, and PUFAs account for 65% of dissimilarity; see also Figure 5b). In contrast, below 250 m small particles are always more refractory, whereas at shallower depths their signature is mixed. This difference between large fresh POM particles and small refractory POM particles at the depths of the mesopelagic particle maxima suggests that the two types of particles may have different ages/origins. Note that, due to the difference in

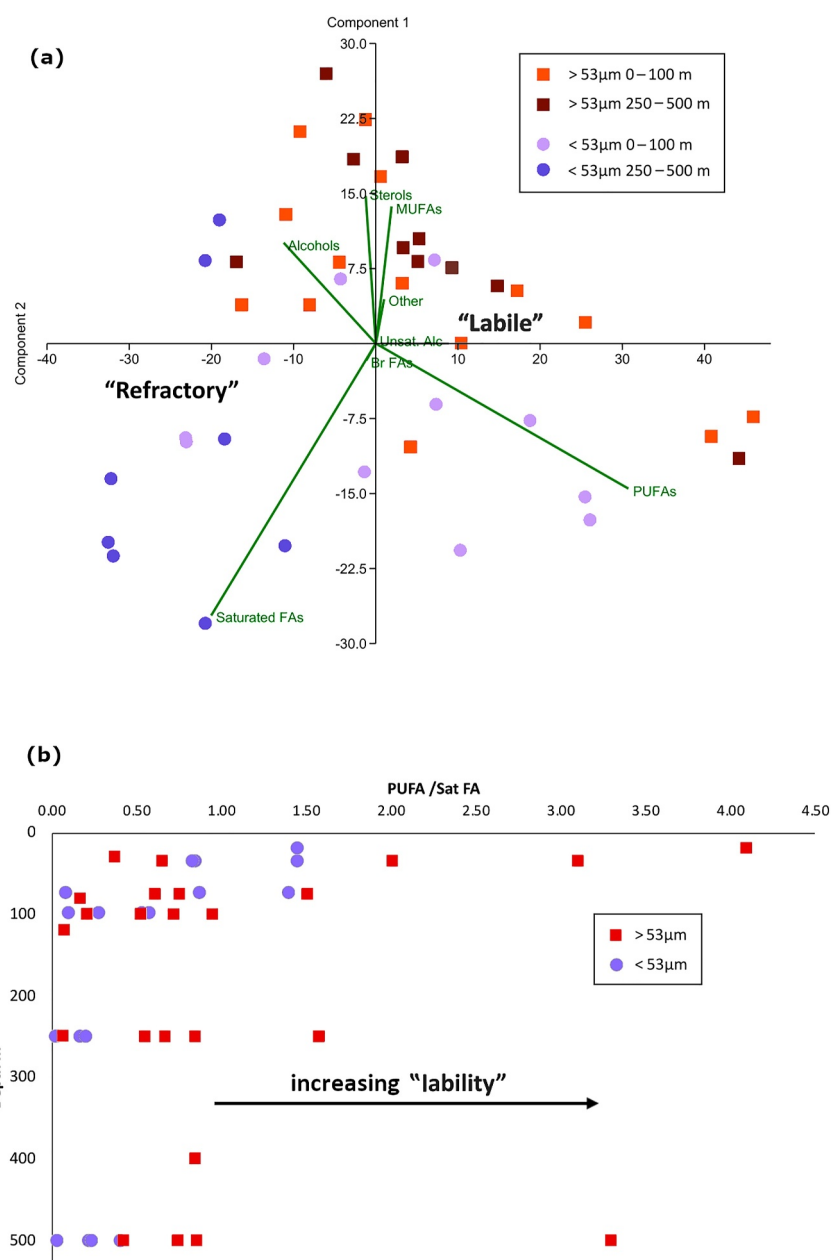


**Figure 5.** (a) Principal component analysis of lipid data for small POM (<53 μm) and large POM (>53 μm) as mol% of compound classes. Saturated FAs - saturated fatty acids; Br Acids—branched fatty acids; PUFAs—polyunsaturated fatty acids; MUFAs—monounsaturated fatty acids; Unsaturated Alcohols—unsaturated alcohols. PC1 and PC2 accounted for 65% of the variance in the data set. (b) PUFA to Saturated fatty acid ratio versus depth.

the cutoff between POM and glider-derived small and large particles, small POM particles represent the lower-end size of the glider-derived small particles.

### 3.3. Biological Sources of Particles Within the OMZ (M1)

#### 3.3.1. Input via Diel Vertical Migration

Acoustic data show clear DVM patterns (Figure 6) with at least three distinct layers that shift from shallower depths at night time to deeper depths during the day time. These layers show DVM patterns that can be described as follows: migrating (a) from the near-surface (night) to above the OMZ (~200 m; day), (b) from between 50 and

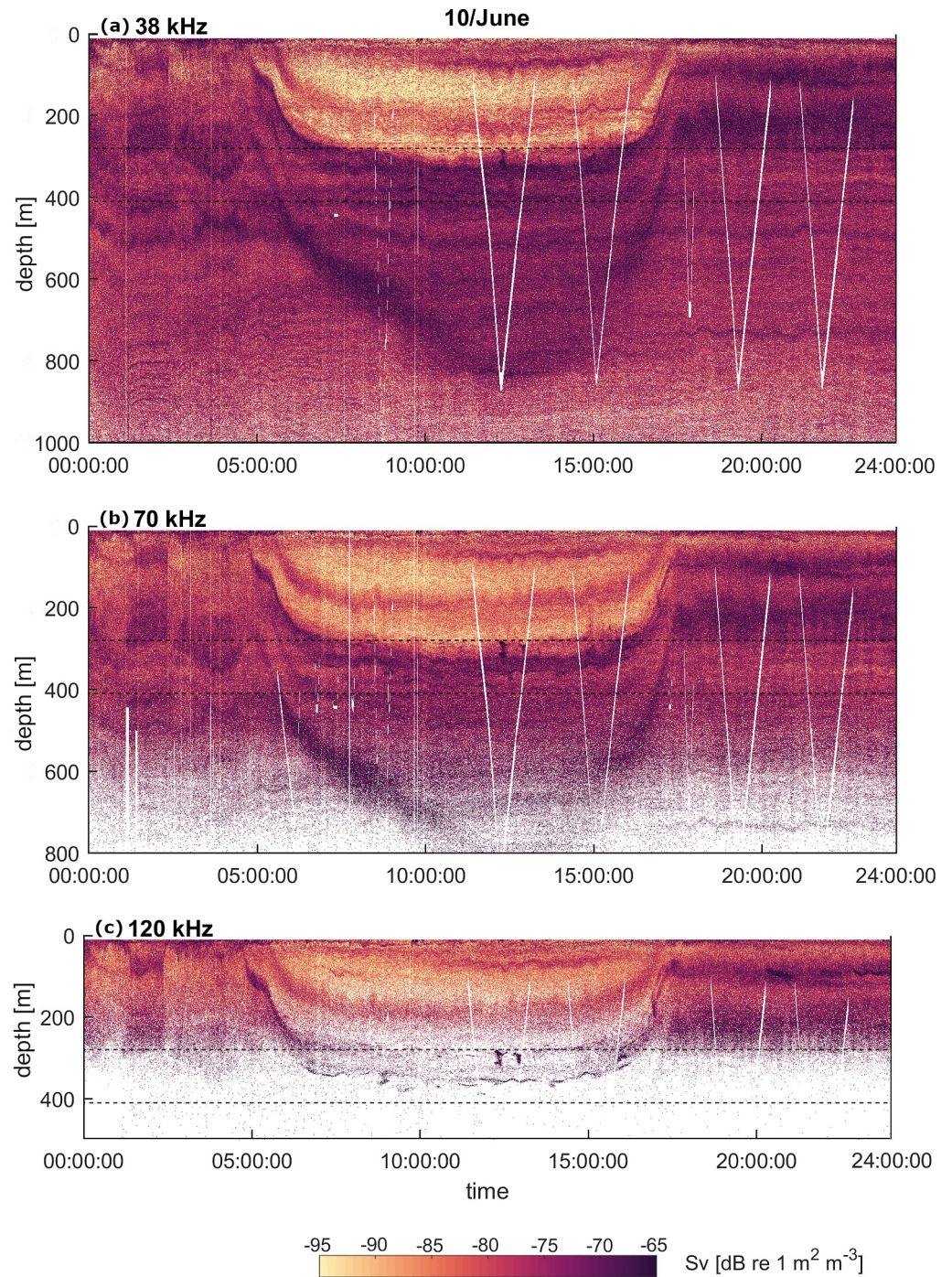


**Figure 6.** Acoustic backscattering data at full resolution for 10 June at (a) 38 kHz, (b) 70 kHz, (c) 120 kHz. Note that higher frequencies can detect smaller organisms. Missing data are indicated in white, including data manually removed to clear noise generated by other measurements collected at the station (e.g., seen as V-shapes). All data are plotted on the same color scale, with darker shades indicating higher acoustic backscattering. Day-night difference plots are provided in Supplement Figure SA4. Dashed lines indicate the depth range spanned by hypoxic waters on 10 June according to CTD data.

150 m depth (night) to the core of the OMZ (350–400 m; day), and (c) from just above the OMZ (~180 to 250 m depth; night) to well below the OMZ (600–850 m; day). The last two patterns are associated with the strongest acoustic backscattering signal. DVM targeting the depth of the OMZ during the day is clearly visible at all frequencies, including the high frequencies that can detect smaller organisms.

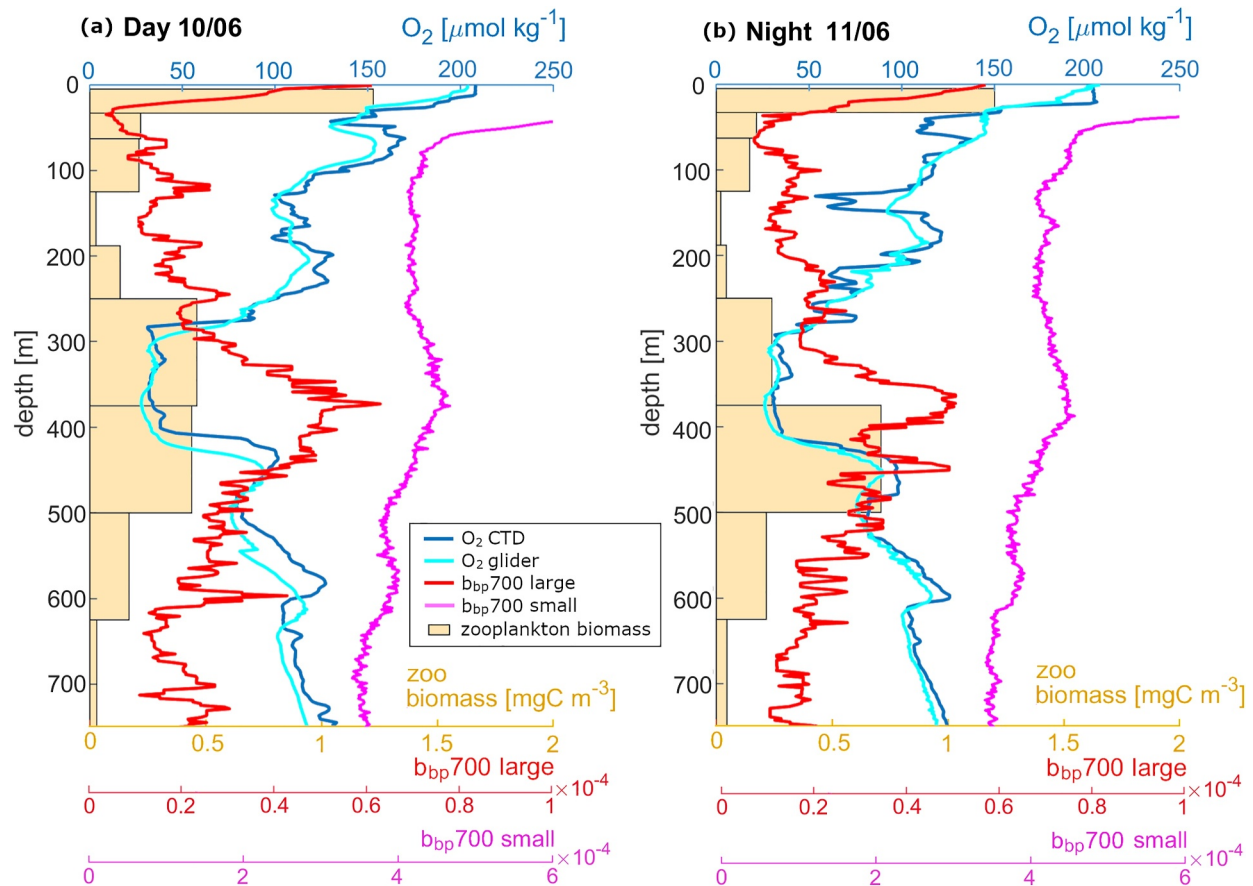


**Figure 7.** Mesozooplankton biomass (0.3–10 mm), oxygen from CTD and glider, and glider large and small particles from optical backscattering ( $b_{bp700}$ ) by depth on (a) 10 June day time and (b) 11 June night time. The width of the zooplankton biomass bins corresponds to the depth intervals spanned by the net for each measurement. Each glider profile represents a 12-hr interval centered around noon or midnight, corresponding to the mean of two 6-hourly glider data bins. In this figure, large (>470  $\mu\text{m}$ ) particle profiles were smoothed using a centered running median filter with a window of 10 bins (20 m) to limit noise. Note that the near-surface small (<470  $\mu\text{m}$ ) particle backscattering is out of scale to allow better visualization of the increase in backscattering at depth. Additional zooplankton data are available in Supplement Figure SA5.

### 3.3.2. Mesozooplankton Residing Within the OMZ

On 10–11 June, ship data indicate that mesozooplankton biomass (300  $\mu\text{m}$ –1 cm size organisms) is high within and below the oxygen minimum, in a depth range of 250–625 m, during both day and night (Figure 7). Minimum mesozooplankton biomass is found between 125 and 250 m, in sub-surface oxygenated waters. During these 2 days, glider and CTD oxygen profiles are very similar, strongly suggesting that glider and ship are sampling within the same waters. Both large and small particles from glider optical backscattering increase with depth below 250 m, approximately following the shape of the mesozooplankton biomass profile up to 625 m and have deep maxima of similar amplitude, despite small particle backscattering having an overall higher signal. A similar correspondence between mesozooplankton biomass as a function of depth and particle abundance is also observed during the night of 6 June, when glider and ship oxygen data similarly coincide (Figure SA6 in Supporting Information S1). Note that camera images suggest that the increase in backscatter is not due to zooplankton itself being detected by the sensor (see Subsection 3.3). The net samples of mesozooplankton biomass shows very little evidence of DVM between the surface and the OMZ (Figure 7).

### 3.4. Transport of Sinking Particles Generated at the Surface (M2)

Model data sub-sampled at the measurement location in February–June shows the signature of the two modeled sinking classes of particulate organic carbon (fast and slow) propagating to depth from the productive layer (Figure 8a). Variability in the lateral currents combined with spatially variable POC allow sinking particle plumes

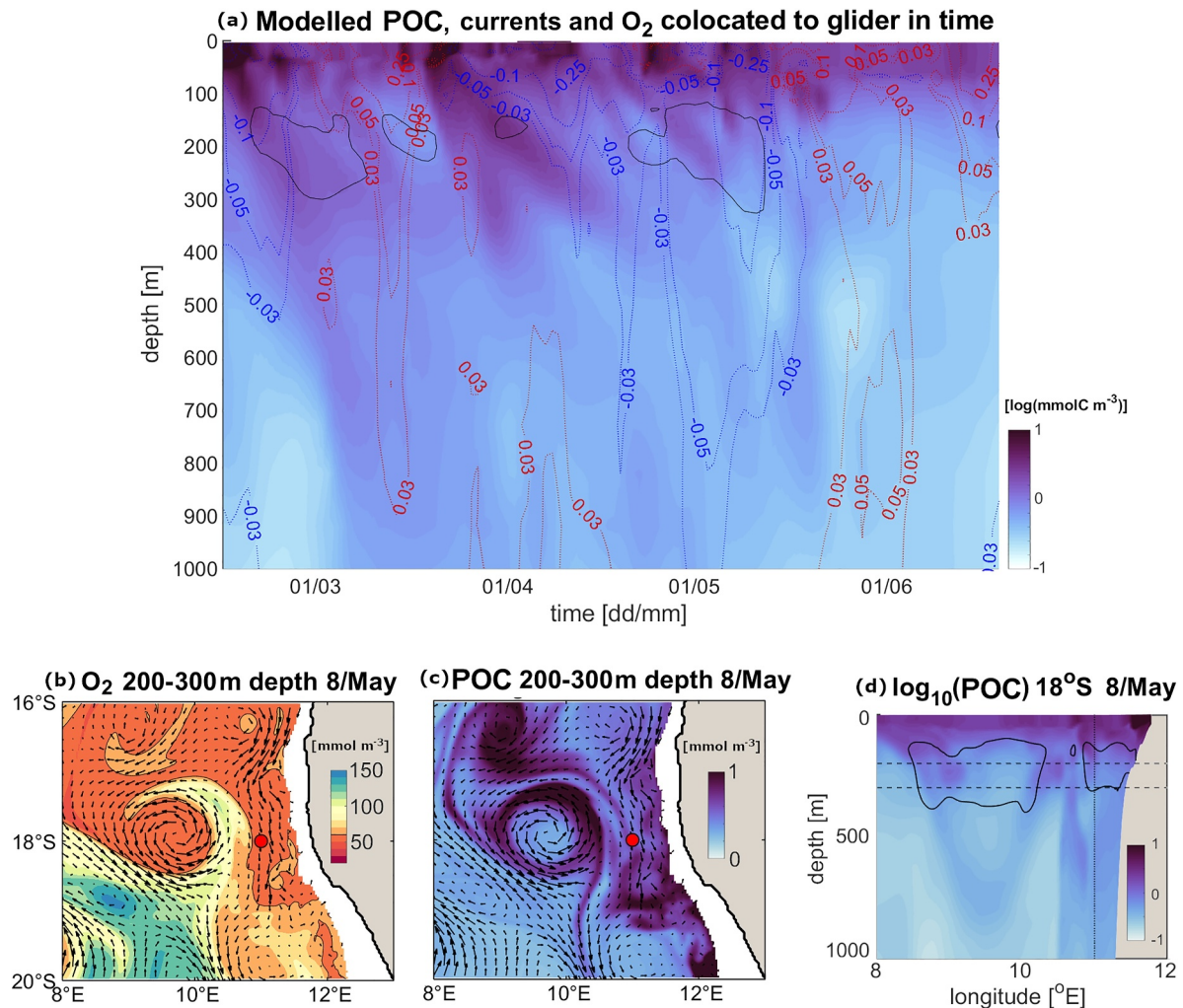


**Figure 8.** Modeled total particulate organic carbon (POC = detrital POC +  $C_{\text{phytoplankton}}$  +  $C_{\text{zooplankton}}$ ), currents and oxygen. (a)  $\log_{10}(C_{\text{org}})$  as a function of depth and time in units of  $\log([\text{mmol m}^{-3}])$  with hypoxic contours ( $O_2 = 60 \text{ mmol m}^{-3}$ ) in black and meridional velocity contours [ $\text{m s}^{-1}$ ] in red (positive, northward) and blue (negative, southward) – all modeled variables in (a) are sampled from the model in the proximity of the glider location ( $11^\circ\text{E}$ ,  $18^\circ\text{S}$ ) from 14 February to 18 June. Subplots (b) and (c) show daily-mean modeled fields averaged between 200 and 300 m depth for 8 May, during the early-May period of strong southward meridional transport and hypoxia in the model, as shown in (a). The white area in (b) and (c) corresponds to the shelf above 200 m (hence no ocean data between 200 and 300 m in that area). (b) Oxygen concentrations [ $\text{mmol m}^{-3}$ ] with hypoxic contours in black ( $O_2 = 60 \text{ mmol m}^{-3}$ ) and horizontal currents (arrows). (c) POC concentration [ $\text{mmol m}^{-3}$ ] with horizontal currents (arrows). (d) Vertical slice of  $\log_{10}(\text{POC})$  at  $18^\circ\text{S}$  on 8 May in units of  $\log([\text{mmol m}^{-3}])$  with hypoxic contours in black ( $O_2 = 60 \text{ mmol m}^{-3}$ ), two horizontal dashed lines mark 200 and 300 m (the depth zone plotted in panels b and c), and the vertical dotted line marks  $11^\circ\text{E}$  (the latitude of the glider observations). Note the typical “wineglass” pattern (Waite et al., 2016) of particles generated by the anticyclonic eddy visible in (b) and (d).

originating from the surface to either intercept the glider position at depth or be flushed away from it, depending on changes in the circulation. This is the case, for example, in mid-May, when high particle concentrations intercept the sampling location at around 700 m depth when the currents change sign (Figure 8a). Nevertheless, in the model output there is no persistent enhancement of particle concentration in a fixed range of depths resembling that of our in situ data, nor do particles increase during modeled hypoxic events. We therefore exclude the lateral transport of particles generated in the productive layer as a likely explanation for the observed mesopelagic particle layers.

### 3.5. Transport of Resuspended Shelf Sediment (M3)

The nearest shelf break from the glider position is found at a distance of  $\sim 50$  km, at about 300 m depth (Figure 1b), similar to the depth of the deep particle layers. According to our model, zonal off-shore currents can maintain speeds of up to  $0.03 \text{ m s}^{-1}$  at 300 m for around 2 weeks, which is just enough time for a parcel of water to

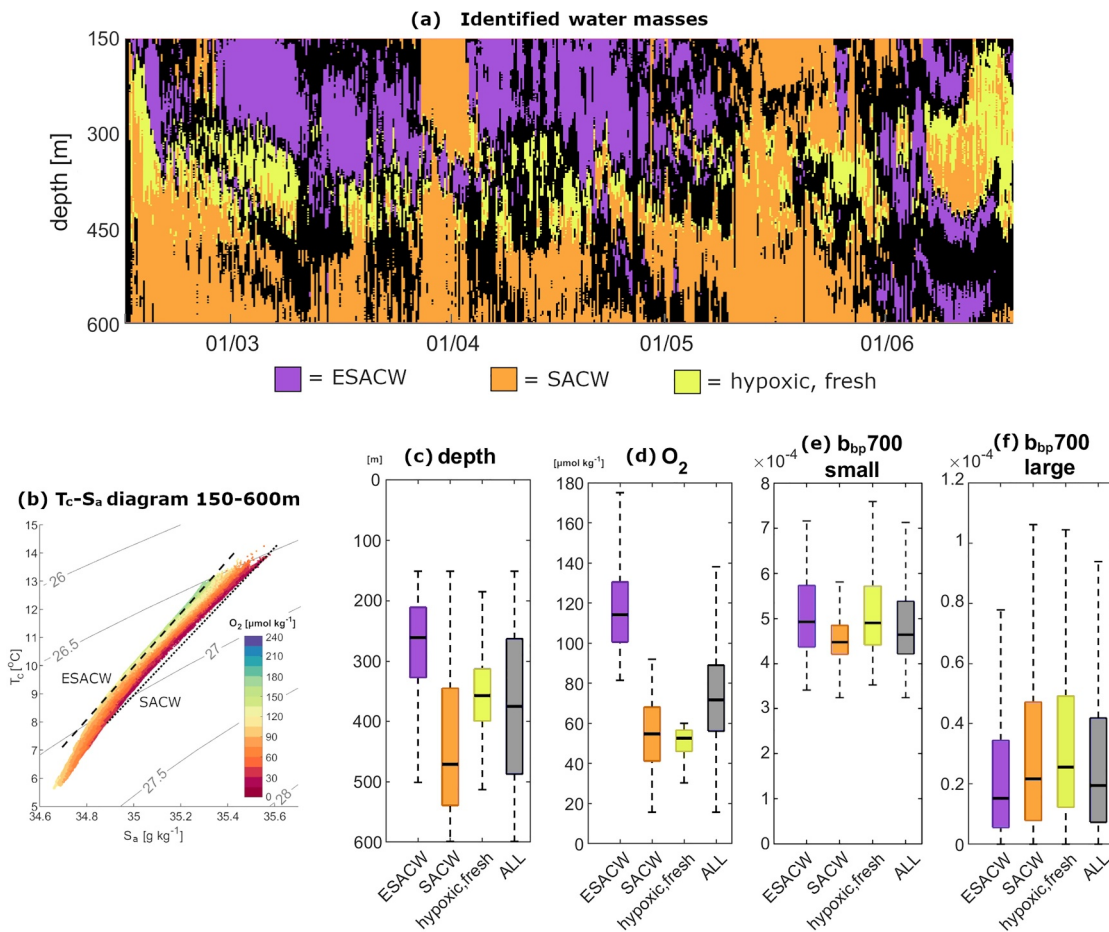


**Figure 9.** (a) Water mass domains as identified from the glider's salinity and oxygen profiles (see Methods), with ESACW in purple, SACW in orange, hypoxic-fresh water in yellow, and undefined water masses in black, the latter representing a mixture of SACW and ESACW with intermediate oxygen and salinity properties. (b) Temperature-salinity diagram for the glider data within 150–600 m depth with water mass characteristic  $T_c$ - $S_a$  lines,  $\sigma_\theta$  isolines in the background (see Methods) and  $O_2$  concentration as color shading. (c)–(f) Water mass properties in the depth range of 150–600 m, with the “ALL” bars referring to the whole set of data in the range of 150–600 m regardless of salinity and oxygen properties: median (horizontal black line), first, and last quartiles (colored bar ranges) and minimum-maximum range (dashed lines). Across all subplots: depth in m, oxygen in  $\mu$ mol kg<sup>-1</sup>.

reach the glider position from the shelf at these speeds. However, cross-shore currents are also characterized by month-long periods of onshore flow (Figure SA6 in Supporting Information S1). It is therefore unlikely that these currents can explain the pattern of deep particles observed at the glider location. Modeled meridional (along-shore) currents are faster (up to  $0.1 \text{ m s}^{-1}$  at 300 m) and meander along the shelf (Figure 8), possibly trapping resuspended sediment en route. However, their pathway to reach the glider is longer, hence also requiring a few weeks to deliver resuspended sediment to the measurement site. In both cases, particles (both large-fresh and small-refractory) need to be suspended in order to reach the glider at 300 m after a few weeks of transport. Deep plumes of sinking particles, as those observed in our glider data, cannot be explained by this mechanism. We elaborate on this further in Discussion Section 4.2.

### 3.6. Physical Drivers of Mesopelagic Particle Variability

Across the 4 months of glider data, deep large- and small-particle layers vary significantly in time with a pattern that is influenced by the time-varying extension of the hypoxic OMZ. Although physical drivers are unlikely to fully explain the origin of the deep particle layers, especially of their sinking component (Sections 3.3 and 3.4), our results suggest that they modulate deep particle concentrations. A comparison of Figures 2 and 9a highlights the similarity of the pattern of alternation of water masses and the temporal fluctuations in deep particle back-scattering as observed in our in situ data. Particle concentrations in relatively deeper SACW waters are

comparable to those of the shallower and oxygenated ESACW (Figures 9c–9f), despite the latter frequently encompassing particles exported from the productive mixed layer.

This water mass alternation is driven by changes in the pattern of currents at the measurement site. According to our model, meridional along-shore currents (Figure 8a) extend deeply into the water column, with speeds up to  $0.05 \text{ m s}^{-1}$  reaching down to 500 m, and change sign on sub-monthly timescales, the same time scales at which central water mass properties vary on our in situ data. Zonal cross-shore currents, on the other hand, have a shallower reach, with currents exceeding  $0.05 \text{ m s}^{-1}$  rarely reaching deeper than 300 m, and vary on slower timescales (see also Figure SA7 in Supporting Information S1). We conclude that alongshore currents, associated with eddy dynamics and with coastal currents that transport ESACW from the south and SACW from the north, are the most likely driver of the modulation of mesopelagic properties on sub-monthly time scales. Zonal currents can also have a role in the transport of dissolved and suspended tracers from the nearshore due to their persistent nature, although on longer timescales. We elaborate on this further in the Discussion.

#### 4. Discussion and Outlook

We used in situ and model data to explore three potential mechanisms of formation for deep particle layers observed in the Benguela hypoxic OMZ: (M1) biological activity within the OMZ; (M2) transport of sinking particles originating from the surface of adjacent productive regions; and (M3) transport of sediment resuspended from the shelf. Our data supports M1, excludes M2 and identifies M3 as a potential but likely partial contribution. In the following subsections we further elaborate on M1 (Section 4.1) and M3 (Section 4.2). We then discuss the role of physics in modulating the deep particle layers (Section 4.3) and discuss implications of our results for ocean biogeochemical models (Section 4.4).

##### 4.1. Hypoxic OMZs: Hotspots of Particle Production and Transformation (M1)

The results of our study show that both biological activity and physical processes shape the deep particle layers observed in the glider data. Biological activity within the OMZ is the most likely mechanism driving the formation of secondary maxima in particle concentrations between 250 and 500 m. Consistent with the results by Rasse and Dall'Olmo (2019), who focused on the North Atlantic hypoxic OMZ, small particles seem to accumulate at the top of the Benguela OMZ for long periods. This sustained accumulation is suggested by the particle's refractory nature at 250 m (Figure 5). Rasse and Dall'Olmo (2019) hypothesize that the persistence of the small particle layers at the top of the hypoxic OMZ of Mauritania may be explained by the in situ production of particles by microbial communities, by analogy with suboxic regions (Gonsalves et al., 2011; Naqvi et al., 1993; Wishner et al., 1995; Wojtasiewicz et al., 2020). For our cruise, however, a preliminary analysis of additional ship data from June showed that prokaryotic (bacteria + archaea) cell counts are about a factor of 6 more abundant in oxygenated waters ( $\text{O}_2 > 100 \mu\text{mol/kg}$ ) than in lower oxygen conditions found within and around Benguela's hypoxic OMZ. This low prokaryotic count, combined with small POM's refractory properties, does not support the microbial production hypothesis. Assuming comparable remineralization rates at all depths, the reduced prokaryotic cell count also suggests that bulk respiration is lower in low-oxygen waters. Incubation experiments based on samples collected during the same cruise also support lower respiration rates in low oxygen waters (Hemsley et al., 2023). These results suggest that: (a) lower microbial respiration may allow for the long-term accumulation of suspended small particles in and around the hypoxic OMZ, and (b) bacterial cell counts do not explain the higher background concentration of small particles observed within hypoxic waters in June.

Although not explaining the deep particle maxima, prokaryotic cell counts in the OMZ fluctuate with the small particle concentration there. In fact, prokaryotic cell counts within hypoxic waters show a small ( $\sim 1.5$  fold) increase on 17 June at 200 m when small particle backscattering in the OMZ also increases between 200 and 350 m (Figure 2, Figure SA2 in Supporting Information S1). Organic carbon measurements from SAPs at 250 m clearly capture the 17 June increase in small particles observed by the glider (Figure SA9 in Supporting Information S1), indicating that they are organic. It is unclear from our data what drives this correlation between fluctuations in particle concentrations and in prokaryotic cell counts in the hypoxic OMZ. Increases in prokaryotic cell counts may be supported by the dissolved nitrogen excreted within the OMZ by mesozooplankton and vertically migrating organisms, which also contribute to deep particle formation. Enhanced prokaryotic activity may also lead to the production of transparent exopolymer particles, which in turn can enhance the formation of large particles via aggregation (Engel et al., 2017). Further studies are needed to investigate these hypotheses.



The bulk of small particles found above and within the OMZ therefore likely either sinks from the productive layer and accumulates at depth due to changes in water density or is generated at depth by particle fragmentation via partial grazing of larger particles (Briggs et al., 2020). A relative increase in the lability of small POM particles at 500 m depth compared to 250 m depth (Figure 5b) indicates that some of the deeper small POM particles (<53  $\mu\text{m}$ ) may originate from fresher large POM particles, which supports the particle fragmentation hypothesis. This hypothesis is also supported by the high mesozooplankton biomass found at 500 m and the similarity between small particle profiles from glider data and the profile of mesozooplankton biomass on 9 and 10 June (Figure 7). Given the sharp decline in both large and small particles between the mixed layer and the OMZ, the question arises about what particles are fed upon and fragmented by zooplankton at depth? One possibility is that large particles are produced directly at depth by organisms performing DVM in sufficient quantities to support the production of small particles via subsequent fragmentation. Another possibility is that especially large (>2 mm) sinking particles such as large phytodetritus aggregates or fecal pellets produced in the mixed layer by macrozooplankton, nekton, and larger organisms, escape the glider data detection due to their large size, fast sinking rates, and sparseness. Nevertheless, these large particles may be intercepted by deep zooplankton communities and fragmented at depth, providing sufficient organic material to generate the observed deep layers. Future studies employing instruments such as underwater vertical profiles (UVPs) and optical sediment traps may be able to better resolve this question.

Large, fast-sinking particles can be produced directly at depth via egestion by both vertically migrating organisms and mesozooplankton communities residing in the OMZ, fueling the observed deep-export events originating from the hypoxic layer. Our acoustic data shows that a portion of migrating organisms move to the OMZ depths during the day, a signal that is visible in every frequency (Figure 6). This broad signal indicates an important role of vertically migrating organisms such as small *euphausiids* (size ~2–3 cm), a type of macrozooplankton that is knowingly abundant in the region (Barange et al., 1991). Among them, *Euphausia hanseni* is known to contribute significantly to DVM, feeding at the surface at night on both phytoplankton and prey such as copepods (Barange et al., 1991; Werner & Buchholz, 2013) and possibly egesting part of this organic material directly into the OMZ during the day. Despite studies indicating that krill can significantly contribute to active export of organic particles (Schnitzer & Steinberg, 2002; Tarling & Johnson, 2006), data regarding egestion rates at depth are still scarce and require to be further investigated.

Data from nets also indicate that non-migratory mesozooplankton communities are abundant in the hypoxic OMZ of the northern Benguela (Figure 7). This observation contrasts with the low biomass observed within the core of suboxic OMZs (Loescher et al., 2016; Hauss et al., 2016), where zooplankton accumulates at the upper and lower OMZ boundaries (Roullier et al., 2014; Wishner et al., 2013). The deep mesozooplankton communities observed in our data likely feed on organic material within the hypoxic OMZ generating a discontinuity in the vertical export pathway of particles: newly egested organic carbon particles most likely differ from those they fed upon in terms of both sinking speed and lability. Furthermore, mesozooplankton living in the OMZ could be subject to predation during the day by diel vertically migrating organisms (Werner & Buchholz, 2013), as previously shown in the Benguela for *Euphausia lucens* (Stuart & Pillar, 1990). Deep predation and subsequent egestion by vertically migrating organisms may constitute an additional source of large particles generated within the OMZ and contributing to both the observed particle layers and deep-export events.

#### 4.2. Contribution From Sediment Resuspension (M3)

Deep particle layers may be generated by the lateral input of sediment originating from the continental shelf (M3), which is known to be rich in organic material (Ma et al., 2021; Marlow et al., 2001). Previous ship-based observations collected in the Benguela at 23°N found particle clouds at 500–600 m at about 150 km from the coast; these clouds showed only a weak connection with the nepheloid layers formed at the shelf break (Inthorn, Mohrholz, & Zabel, 2006). Nevertheless, the authors did not exclude a shelf origin of the particles. Organic carbon rich sediment found on the Benguela shelf can be resuspended by a combination of bioturbation and physical processes (Boegman & Stastna, 2019; Inthorn, Wagner, et al., 2006; Monteiro et al., 2005) and is known to be advected laterally, predominantly within bottom nepheloid layers (Mollenhauer et al., 2007). In principle, part of this sediment may be trapped by deep-reaching lateral currents and advected further offshore.

We cannot fully exclude some contribution of shelf sediment resuspension to the deep particle layer formation, at least to their suspended component. However, this formation mechanism does not explain how large, fresh and

sinking particles can originate from the OMZ, due to the time needed to advect them from the shelf (Section 3.5). Biological activity within the hypoxic OMZ on the other hand, provides a stronger explanation for the origin of both small and large particle layers. The sediment resuspension mechanism remains therefore a partial explanation of the deep particle layers formation. Future studies could further investigate this mechanism with particle tracking algorithms.

### 4.3. Understanding the Role of Physics: Lateral Fluxes and Biophysical Interactions

The results of our study show that lateral advection of water masses and tracers modulate the intensity of deep particle layers (both large and small particles) in the hypoxic northern Benguela. This conclusion is in line with previous research, showing that deep particle layers in OMZs can occasionally be interrupted by intrusions of fresher and more oxygenated waters with low particle concentrations (Ulloa et al., 2012). Since oxygenated ESACW is found in the northern Benguela mostly in Austral winter (Muller et al., 2014; Siegfried et al., 2019), deep particle layers associated with the OMZ may also exhibit seasonal variability. Small particles, microbial communities and, to a certain extent, zooplankton, act as passive tracers and may therefore be advected laterally within water masses, hence making it necessary to consider lateral transports when studying the biological carbon pump. These results are consistent with previous literature highlighting the three-dimensional nature of the biological pump (Frischknecht et al., 2018; Lovecchio et al., 2017; Mollenhauer et al., 2007) and highlight that part of the lateral transport of particulate organic carbon takes place below the productive layer, in the upper mesopelagic. Better understanding the fate of this mobile mesopelagic layer of particulate organic carbon and the associated fluxes is key to resolving the organic carbon cycle of OMZs, especially at the boundary of coastal upwelling systems.

The variability in large particle concentrations sinking rapidly out of hypoxic waters instead highlights the quick organic carbon turnover within the OMZ and the fast response of biological activity to the presence or absence of hypoxia. Increases in large particles sinking out of the hypoxic layer are visible in early March, late April, and early to mid-May and again in June (Figure 2) and hence constitute a recurrent feature of the hypoxic OMZ. An outstanding deep export event that differs in intensity from the others captured by the glider is observed during 10–20 May. During this period, glider data show a sudden increase in small and large mesopelagic particles between 150 and 500 m depth (Figure 2). In the same depth range, salinity increases and oxygen drops to values typical of SACW (Figure 9a), most likely due to currents flushing saline and O<sub>2</sub>-poor water from the north toward the glider (Figures 8b–8d; see also Lovecchio et al., 2022). From the OMZ to at least 1,000 m depth, the glider detects an intense and deep flux of large particles, and a high fluorescence signal indicating fresh sinking particles (Figure SA3b in Supporting Information S1). These large, fast-sinking and fresh particles suddenly appear within the OMZ. Two mechanisms might explain this sudden deep export event. Particles may originate from a sinking plume trapped and laterally advected by deep-reaching currents associated with small-scale variability (see mid-May satellite data in Figure SA8 in Supporting Information S1), as sporadically observed in our model (Figure 8a). Alternatively, these fast-sinking and fresh particles may be produced directly at depth by biological activity, as suggested by the association between hypoxic waters and the origin of the plume. Crucially, this deep-export event is also observed just after mixed layer fluorescence reaches a peak (Figure SA3b in Supporting Information S1). Further studies should aim at capturing and investigating the biophysical interactions driving these sporadic and intense deep sinking events.

The biological response to changes in the depth range and severity of hypoxia may involve changes in remineralization rates (Hemsley et al., 2023), rapid shifts in the vertical distribution of zooplankton, and changes in the pattern of DVM. We do not have sufficient data to address changes in the distribution of zooplankton biomass following shifts in the shape of the OMZ. The analysis of day-night differences in acoustic backscattering suggests that, whereas DVM takes place regardless of the shape of the hypoxic OMZ, the depth and width of the day-night maximum and minimum change with the expansion of the hypoxic region (Figure SA5 in Supporting Information S1). This observation indicates that DVM may be adjusting to some extent to changes in the OMZ. Subsurface mesoscale eddies with extreme hypoxic conditions (O<sub>2</sub> < 30 μmol kg<sup>-1</sup>) traveling across the Benguela region, such as the one observed across the beginning of April between 75 and 300 m (Figure 2 and Figure SA1 in Supporting Information S1, see also Lovecchio et al., 2022), can also disrupt zooplankton activity in the mesopelagic. A subsurface eddy in the North Atlantic OMZ with similar oxygen concentrations was observed to trigger a halt in zooplankton's DVM and to possibly induce zooplankton to escape toward less extreme oxygen conditions (Karstensen et al., 2015). Since we identified zooplankton activity as one of the key drivers of the

generation of deep particle layers, changes in zooplankton behavior could generate anomalies in the deep particle concentrations compared to the mean OMZ's pattern. Future studies should focus on how the dynamics of the different trophic levels respond to short-term variability in hypoxia and how this impacts organic carbon fluxes across the mesopelagic.

#### 4.4. Modeling the Organic Carbon Cycle of Hypoxic OMZs

In the present study, we used the output of a coupled physical-biogeochemical model to better understand the drivers of variability of the deep particle layers and identify their origin. Despite the relevant insight provided by the simulations with regards to currents, water masses, and oxygen variability, our biogeochemical model failed to reproduce the observed mesopelagic particle layers. The BEC biogeochemical model employed in the present study (Frischknecht et al., 2018; Moore et al., 2013) does not include processes such as particle fragmentation, DVM, an explicit representation of heterotrophic bacteria (to be precise, prokaryotes) or POC resuspension, which our results indicate may work in synergy to build up the deep particle concentrations observed in hypoxic water. The BEC model's representation of the marine organic carbon cycle is comparable to other biogeochemical models employed in regional and climate simulations (e.g., S  f  rian et al., 2020), hence suggesting that none of these models would be able to reproduce such deep particle layers. The large (and expanding) area covered by hypoxic ocean regions and the importance of correctly representing the organic carbon cycle in Earth System Models used for climate projections points to the necessity of improving understanding and representation of biological carbon pump processes occurring in OMZs. Our results based on in situ data clearly indicate that simplified representations of the biological pump that ignore particle transformations across the water column, such as the Martin curve model (Martin et al., 1987), are unlikely to apply to hypoxic OMZs. Our model results further suggest that even an explicit representation of sinking detritus may also not be sufficient and that models may need to account for some additional biological processes to improve their performance in these regions.

Recent efforts aimed at including DVM in physical-biogeochemical coupled ocean models have been successful at reproducing the observed migratory patterns and capturing the relative biomass of migrating organisms (Aumont et al., 2018; Bianchi et al., 2013). More observations are needed to better understand, and hence better model, the regional and spatiotemporal variability of DVM (Bandara et al., 2021). Other improvements in zooplankton modeling include accounting for their role in particle fragmentation. A recent development in this direction has been including particle-associated copepods in a branch of the biogeochemical model MEDUSA, which significantly improved modeled POC fluxes (Mayor et al., 2020; Palmi  ri et al., 2021). Refining the representation of heterotrophic bacteria (i.e., prokaryotes) and remineralization rates has also proven successful at better representing OMZs in models (Laufk  tter et al., 2017; Lovato et al., 2022; S  f  rian et al., 2020); further improvements in this direction may be fundamental to simulate particle dynamics in OMZs. Sediment modules are mostly employed in the context of modeling coastal oceans (Almroth-Rosell et al., 2011; Sherwood et al., 2018; Wainright & Hopkinson Jr, 1997); these modules are computationally expensive, and their performance depends on fine topographic details and small-scale physical processes (Boegman & Stastna, 2019; Monteiro et al., 2005). Parameterizing these processes may be necessary to include them in global models, if sediment resuspension is proven to be a globally significant source of organic carbon for the mesopelagic.

Improving the representation of particle distributions in OMZs may prove fundamental also in improving the representation of the oxygen cycle in global models. These models are known to perform poorly in representing the volume of low oxygen regions and show little agreement on oxygen trends both between each other and compared with in situ observations (Cabr   et al., 2015; Ito et al., 2017; Oschlies et al., 2018). Crucially, the representation of the Atlantic hypoxic OMZs has not significantly improved between CMIP5 and CMIP6 simulations, and hypoxia remains poorly represented in most models (S  f  rian et al., 2020). Focusing on better representing the biogeochemical transformations taking place in the hypoxic OMZ and, more broadly, in the mesopelagic may therefore be a necessary step to develop the future generation of biogeochemical ocean models.

### 5. Summary and Outlook

We examined three potential mechanisms (M) for the generation of deep particle layers in the Benguela OMZ. Our study finds that mesopelagic particle layers in the offshore northern Benguela are most plausibly generated by biological processes such as DVM and zooplankton activity within hypoxic waters (M1, Sections 3.2, 3.3 and

4.1). Our results do not support formation of the deep layers via the lateral transport of sinking particles generated at the surface in adjacent highly productive regions (M2, Section 3.4). Shelf sediment resuspension can only provide a partial explanation to the formation of the deep particle layers, since it only allows suspended particles to reach the glider position, and so it cannot explain the observed deep sinking plumes (M3, Sections 3.5 and 4.2). The temporal variability in the deep particle concentrations is further modulated by lateral currents that drive changes in the shape and intensity of the OMZ core (Sections 3.6 and 4.3).

Our results highlight that hypoxic OMZs are hotspots of organic carbon transformation and impact particle fluxes across the mesopelagic. A few questions remain open. More studies are needed to understand the relative role of zooplankton targeting the hypoxic layer to: (a) escape predators; (b) feeding on preexisting suspended particles as well as large particles sinking from above. Our data indicate that all these processes are relevant for the formation and transformation of particles in the OMZ, but their relative contribution must be quantified. Biological responses to sub-monthly changes in the depth, thickness, and intensity of the OMZ layer, such as changes in the depth of DVM, should be further investigated. The role of microbial activity in the OMZ also needs to be further clarified: although we can exclude that deep particle layers are constituted predominantly of microbial biomass, we cannot exclude that organic byproducts of microbial activity accumulate in the OMZ and contribute to particle formation. Better understanding of these processes is needed prior to developing parameterizations and correction factors to account for the way hypoxic OMZs affect the marine organic carbon cycle at depth. Future models aimed at improving representation of the biogeochemistry of hypoxic OMZs (Section 4.4) may need to account for some of these processes.

### Conflict of Interest

The authors declare no conflicts of interest relevant to this study.

### Data Availability Statement

Binned glider data used for this study are available on PANGAEA at Lovecchio et al. (Dataset, 2023) and Lovecchio et al. (Dataset, 2025). Ship data such as dissolved oxygen and mammoth net data from cruise DY090 can be accessed via the British Oceanographic Data Center (BODC COMICS data). POM organic geochemistry data are provided with this manuscript, in Supplement D. Model data are available on PANGAEA in Lovecchio (Dataset, 2025). Other publicly available data sets used for this study are referenced in our Bibliography as: CMEMS GlobColour, CMEMS GlobCurrent, CMEMS DUACS, CMEMS GLORYS, ESA-CCI Surface Salinity, GEBCO 2021, Modis Aqua, NASA-OBPG SeaWiFS (2014), WOA2018 Oxygen, WOA2023 Salinity.

We thank the officers, crew, and technicians from the Namibian Ministry of Fisheries on board R/V Mirabilis for their assistance in deploying the gliders.

### References

- Almroth-Rosell, E., Eilola, K., Hordoir, R., Meier, H. M., & Hall, P. O. (2011). Transport of fresh and resuspended particulate organic material in the baltic sea—A model study. *Journal of Marine Systems*, 87(1), 1–12. <https://doi.org/10.1016/j.jmarsys.2011.02.005>
- Aumont, O., Maury, O., Lefort, S., & Bopp, L. (2018). Evaluating the potential impacts of the diurnal vertical migration by marine organisms on marine biogeochemistry. *Global Biogeochemical Cycles*, 32(11), 1622–1643. <https://doi.org/10.1029/2018GB005886>
- Bandara, K., Varpe, Ø., Wijewardene, L., Tverberg, V., & Eiane, K. (2021). Two hundred years of zooplankton vertical migration research. *Biological Reviews*, 96(4), 1547–1589. <https://doi.org/10.1111/brv.12715>
- Barange, M., Gibbons, M. J., & Carola, M. (1991). Diet and feeding of *Euphausia hansenii* and *nematoscelis megalops* (Euphausiacea) in the northern Benguela current: Ecological significance of vertical space partitioning. *Marine Ecology Progress Series*, 73(2/3), 173–181. <https://doi.org/10.3354/meps073173>
- Bianchi, D., Stock, C., Galbraith, E. D., & Sarmiento, J. L. (2013). Diel vertical migration: Ecological controls and impacts on the biological pump in a one-dimensional ocean model. *Global Biogeochemical Cycles*, 27(2), 478–491. <https://doi.org/10.1002/gbc.20031>
- BODC COMICS data [Dataset]. The oceanographic dataset collected during the controls over Ocean Mesopelagic interior carbon storage (COMICS) project (2017–2022), Retrieved from <https://www.bodc.ac.uk/resources/inventories/edmed/report/6725/> (last accessed 16 October 2024).
- Boegman, L., & Stastna, M. (2019). Sediment resuspension and transport by internal solitary waves. *Annual Review of Fluid Mechanics*, 51(1), 129–154. <https://doi.org/10.1146/annurev-fluid-122316-045049>
- Boyer, T. P., Garcia, H. E., Locarnini, R. A., Zweng, M. M., Mishonov, A. V., Reagan, J. R., et al. (2018). *World Ocean Atlas 2018. Salinity*. NOAA National Centers for Environmental Information. Dataset. Retrieved from <https://www.ncei.noaa.gov/archive/accession/NCEI-WOA18>
- Briggs, N., Dall'Olmo, G., & Claustre, H. (2020). Major role of particle fragmentation in regulating biological sequestration of CO<sub>2</sub> by the oceans. *Science*, 367(6479), 791–793. <https://doi.org/10.1126/science.aay1790>

### Acknowledgments

The authors would like to thank Dr Anita Flohr for her precious feedback and Dr Claire Evans for her contribution. A great thanks goes to Dr Matthias Münnich for his help and technical support and Dr Flora Desmet for her suggestions. We thank Prof Geraint Tarling and Dr Gabriele Stowasser for their time and precious insight. We thank the officers, crew, and technicians from the Namibian Ministry of Fisheries on board R/V Mirabilis and the officers, crew and DY090 science team on board RRS Discovery for the successful cruise operations and the deployment and recovery of the glider. We also thank the NOC Marine Autonomous Robotic Systems (MARS) team for their support in the preparation and piloting of the glider. This research was financially supported by a European Research Council Consolidator Grant (GOCART, agreement number 724416), by the Natural Environment Research Council through the COMICS project (Controls over Ocean Mesopelagic Interior Carbon Storage; NE/M020835/1; NE/M020835/2; NE/M020878/1; NE/M020762/1) and by the Swiss National Science Foundation (SNSF Grant P2EZP2\_184251).

- Briggs, N., Perry, M. J., Cetinić, I., Lee, C., D'Asaro, E., Gray, A. M., & Rehm, E. (2011). High-resolution observations of aggregate flux during a sub-polar North Atlantic spring bloom. *Deep Sea Research Part I: Oceanographic Research Papers*, 58(10), 1031–1039. <https://doi.org/10.1016/j.dsr.2011.07.007>
- Cabr , A., Marinov, I., Bernardello, R., & Bianchi, D. (2015). Oxygen minimum zones in the tropical Pacific across CMIP5 models: Mean state differences and climate change trends. *Biogeosciences*, 12(18), 5429–5454. <https://doi.org/10.5194/bg-12-5429-2015>
- Cavan, E., Trimmer, M., Shelley, F., & Sanders, R. (2017). Remineralization of particulate organic carbon in an ocean oxygen minimum zone. *Nature Communications*, 8(1), 14847. <https://doi.org/10.1038/ncomms14847>
- CMEMS DUACS [Dataset]. Global Ocean gridded L 4 sea surface heights and derived variables reprocessed 1993 ongoing. Product ID: SEALEVEL\_GLO\_PHY\_L4\_MY\_008\_047. <https://doi.org/10.48670/moi-00148>
- CMEMS GlobColour [Dataset]. Global Ocean colour (Copernicus-GlobColour), bio-geo-chemical, L3 (daily) from satellite observations (1997-ongoing). Product ID: OCEANCOLOUR\_GLO\_BGC\_L3\_MY\_009\_103. <https://doi.org/10.48670/moi-00280>
- CMEMS GlobCurrent [Dataset]. Global total (COPERNICUS-GLOBCURRENT), Ekman and geostrophic currents at the surface and 15m. Product ID: MULTIOBS\_GLO\_PHY\_MYNRT\_015\_003. <https://doi.org/10.48670/mds-00327>
- CMEMS GLORYS [Dataset]. Global Ocean Physics Reanalysis, 1/12° horizontal resolution, 50 vertical levels. Product ID: GLOBAL\_MULTITYEAR\_PHY\_001\_030. <https://doi.org/10.48670/moi-00021>
- Dalsgaard, J., St. John, M., Kattner, G., M ller-Navarra, D., & Hagen, W. B. T.-A. (2003). *Fatty acid trophic markers in the pelagic marine environment* (pp. 225–340). Academic Press. [https://doi.org/10.1016/S0065-2881\(03\)46005-7](https://doi.org/10.1016/S0065-2881(03)46005-7)
- de Froe, E., Horn, H., Wolff, G. A., Blackbird, S., Mohn, C., Maier, S., et al. (2022). Food distribution during a tidal cycle across a cold-water coral mound. *Deep-Sea Research I – Oceanographic Research Papers*, 189, 108354. <https://doi.org/10.1016/j.dsr.2022.103854>
- Demer, D. A., Berger, L., Bernasconi, M., Bethke, E., Boswell, K., Chu, D., et al. (2015). Calibration of acoustic instruments. ICES Cooperative Research Report No., 326, 133. <https://repository.oceanbestpractices.org/handle/11329/626>
- Deutsch, C., Brix, H., Ito, T., Frenzel, H., & Thompson, L. (2011). Climate-forced variability of ocean hypoxia. *Science*, 333(6040), 336–339. <https://doi.org/10.1126/science.1202422>
- Duineveld, G., Jeffreys, R., Lavaleye, M., Davies, A., Bergman, M., Watmough, T., & Witbaard, R. (2012). Spatial and tidal variation in food supply to shallow cold-water coral reefs of the Mingulay Reef complex (Outer Hebrides, Scotland). *Marine Ecology Progress Series*, 444, 97–115. <https://doi.org/10.3354/meps09430>
- Dussin, R., Barnier, B., & Brodeau, L. (2016). “The making of Drakkar forcing set DFS5” *DRAKKAR/MyOcean Report 01-04-16*, LGGE, Retrieved from [https://www.drakkar-ocean.eu/publications/reports/report\\_DFS5v3\\_April2016.pdf](https://www.drakkar-ocean.eu/publications/reports/report_DFS5v3_April2016.pdf) (last accessed 21/August/2023)
- Ekau, W., Auel, H., P rtner, H.-O., & Gilbert, D. (2010). Impacts of hypoxia on the structure and processes in pelagic communities (zooplankton, macro-invertebrates and fish). *Biogeosciences*, 7(5), 1669–1699. <https://doi.org/10.5194/bg-7-1669-2010>
- Engel, A., Wagner, H., Le Moigne, F. A. C., & Wilson, S. T. (2017). Particle export fluxes to the oxygen minimum zone of the eastern tropical North Atlantic. *Biogeosciences*, 14(7), 1825–1838. <https://doi.org/10.5194/bg-14-1825-2017>
- ESA-CCI Surface Salinity [Dataset]. ESA CCI Sea Surface Salinity ECV produced at a spatial resolution of 50 km and time resolution of 1 month and spatially resampled on 25 km EASE grid and 15 days of time sampling. <https://doi.org/10.5285/5920a2c77e3c45339477acd31ce62c3c>
- Francois, R. S., & Garrison, G. R. (1982). Sound absorption based on ocean measurements. Part II: Boric acid contribution and equation for total absorption. *Journal of the Acoustical Society of America*, 72(6), 1879–1890. <https://doi.org/10.1121/1.388673>
- Frischknecht, M., M nnich, M., & Gruber, N. (2018). Origin, transformation, and fate: The three-dimensional biological pump in the California Current System. *Journal of Geophysical Research: Oceans*, 123(11), 7939–7962. <https://doi.org/10.1029/2018JC013934>
- Ganesh, S., Bristow, L., Larsen, M., Sarode, N., Thamdrup, B., & Stewart, F. J. (2015). Size-fraction partitioning of community gene transcription and nitrogen metabolism in a marine oxygen minimum zone. *ISME Journal*, 9(12), 2682–2696. <https://doi.org/10.1038/ismej.2015.44>
- Garcia, H. E., Boyer, T. P., Baranova, O. K., Locarnini, R. A., Mishonov, A. V., Grodsky, A., et al. (2019). *World Ocean Atlas 2018: Product documentation*. A. Mishonov, Technical Editor, Retrieved from <https://www.ncei.noaa.gov/data/oceans/wao/WOA18/DOC/wao18documentation.pdf> (last accessed: 21 August 2023)
- Garfield, P. C., Packard, T. T., Friederich, G. E., & Codispoti, L. A. (1983). A subsurface particle maximum layer and enhanced microbial activity in the secondary nitrite maximum of the northeastern tropical Pacific Ocean. *Journal of Marine Research*, 41(4), 747–768. <https://doi.org/10.1357/002224083788520496>
- GEBCO. (2021). The GEBCO\_2021 Grid - A continuous terrain model for oceans and land at 15 arc-second intervals. [Dataset]. <https://doi.org/10.5285/c6612cbe-50b3-0cff-e053-6c86abc09f8f>
- Giering, S. L. C., Wells, S. R., Mayers, K. M. J., Hanna, S., Cornwell, L., Fileman, E. S., et al. (2019). Seasonal variation of zooplankton community structure and trophic position in the Celtic sea: A stable isotope and biovolume spectrum approach. *Progress in Oceanography*, 177, 101943. <https://doi.org/10.1016/j.pocean.2018.03.012>
- Gonsalves, M. J., Paropkari, A. L., Fernandes, C. E. G., Bharathi, P. L., Krishnakumari, L., Fernando, V., & Nampoothiri, G. E. (2011). Pre-dominance of anaerobic bacterial community over aerobic community contribute to intensify ‘oxygen minimum zone’ in the eastern Arabian Sea. *Continental Shelf Research*, 31(11), 1224–1235. <https://doi.org/10.1016/j.csr.2011.04.011>
- Gowing, M. M., & Wishner, K. F. (1992). Feeding ecology of benthopelagic zooplankton on an eastern tropical Pacific seamount. *Marine Biology*, 112(3), 451–467. <https://doi.org/10.1007/BF00356291>
- Hauss, H., Christiansen, S., Sch tte, F., Kiko, R., Edvam Lima, M., Rodr guez, E., et al. (2016). Dead zone or oasis in the open ocean? Zooplankton distribution and migration in low-oxygen medowater eddies. *Biogeosciences*, 13(6), 1977–1989. <https://doi.org/10.5194/bg-13-1977-2016>
- Hemsley, V., F ssel, J., Duret, M. T., Rayne, R. R., Iversen, M. H., Henson, S. A., et al. (2023). Suspended particles are hotspots of microbial remineralization in the ocean’s twilight zone. *Deep Sea Research Part II: Topical Studies in Oceanography*, 212, 105339. <https://doi.org/10.1016/j.dsr2.2023.105339>
- Henson, S. A., Briggs, N., Carvalho, F., Manno, C., Mignot, A., & Thomalla, S. (2023). A seasonal transition in biological carbon pump efficiency in the northern Scotia Sea, Southern Ocean. *Deep Sea Research Part II: Topical Studies in Oceanography*, 208, 105274. <https://doi.org/10.1016/j.dsr2.2023.105274>
- Hersbach, H., Bell, B., Berrisford, P., Biavati, G., Hor nyi, A., M n oz Sabater, J., et al. (2023). ERA5 hourly data on single levels from 1940 to present. *Copernicus Climate Change Service (C3S) Climate Data Store (CDS)*. <https://doi.org/10.24381/cds.adbb2d47>
- Inthorn, M., Mohrholz, V., & Zabel, M. (2006). Nepheloid layer distribution in the Benguela upwelling area offshore Namibia. *Deep Sea Research Part I: Oceanographic Research Papers*, 53(8), 1423–1438. <https://doi.org/10.1016/j.dsr.2006.06.004>
- Inthorn, M., Wagner, T., Scheeder, G., & Zabel, M. (2006). Lateral transport controls distribution, quality, and burial of organic matter along continental slopes in high-productivity areas. *Geology*, 34(3), 205–208. <https://doi.org/10.1130/G22153.1>

- Ito, T., Minobe, S., Long, M. C., & Deutsch, C. (2017). Upper ocean O<sub>2</sub> trends: 1958–2015. *Geophysical Research Letters*, *44*(9), 4214–4223. <https://doi.org/10.1002/2017GL073613>
- Kalvelage, T., Jensen, M. M., Contreras, S., Revsbech, N. P., Lam, P., Günter, M., et al. (2011). Oxygen sensitivity of anammox and coupled N-cycle processes in oxygen minimum zones. *PLoS One*, *6*(12), e29299. <https://doi.org/10.1371/journal.pone.0029299>
- Kara, A. B., Rochford, P. A., & Hurlburt, H. E. (2003). Mixed layer depth variability over the global ocean. *Journal of Geophysical Research*, *108*(C3), 3079. <https://doi.org/10.1029/2000jc000736>
- Karstensen, J., Fiedler, B., Schütte, F., Brandt, P., Körtzinger, A., Fischer, G., et al. (2015). Open ocean dead zones in the tropical North Atlantic Ocean. *Biogeosciences*, *12*(8), 2597–2605. <https://doi.org/10.5194/bg-12-2597-2015>
- Karstensen, J., Stramma, L., & Visbeck, M. (2008). Oxygen minimum zones in the eastern tropical Atlantic and Pacific oceans. *Progress in Oceanography*, *77*(4), 331–350. ISSN 0079-6611. <https://doi.org/10.1016/j.pocean.2007.05.009>
- Keeling, R. F., Körtzinger, A., & Gruber, N. (2010). Ocean deoxygenation in a warming world. *Annual Review of Marine Science*, *2*(1), 199–229. <https://doi.org/10.1146/annurev.marine.010908.163855>
- Keil, R. G., Neibauer, J. A., Biladeau, C., van der Elst, K., & Devol, A. H. (2016). A multiproxy approach to understanding the “enhanced” flux of organic matter through the oxygen-deficient waters of the Arabian Sea. *Biogeosciences*, *13*(7), 2077–2092. <https://doi.org/10.5194/bg-13-2077-2016>
- Kiriakoulakis, K., Bett, B. J., White, M., & Wolff, G. A. (2004). Organic biogeochemistry of the Darwin Mounds, a deep-water coral ecosystem, of the NE Atlantic. *Deep Sea Research Part I: Oceanographic Research Papers*, *51*(12), 1937–1954. <https://doi.org/10.1016/j.dsr.2004.07.010>
- Köhn, E. E., Münnich, M., Vogt, M., Desmet, F., & Gruber, N. (2022). Strong habitat compression by extreme shoaling events of hypoxic waters in the Eastern Pacific. *Journal of Geophysical Research: Oceans*, *127*(6), e2022JC018429. <https://doi.org/10.1029/2022JC018429>
- Laffoley, D., & Baxter, J. M. (2019). *Ocean deoxygenation: Everyone's problem: Causes, impacts, consequences and solutions: Summary for Policy Makers*. International Union for Conservation of Nature (IUCN). Retrieved from <https://portals.iucn.org/library/sites/library/files/documents/2019-048-En.pdf> (last accessed 15/Dec/2023)
- Landschützer, P., Gruber, N., Bakker, D. C. E., Schuster, U., Nakaoka, S., Payne, M. R., et al. (2013). A neural network-based estimate of the seasonal to inter-annual variability of the Atlantic Ocean carbon sink. *Biogeosciences*, *10*(11), 7793–7815. <https://doi.org/10.5194/bg-10-7793-2013>
- Large, W. G., McWilliams, J. C., & Doney, S. C. (1994). Oceanic vertical mixing: A review and a model with a nonlocal boundary layer parameterization. *Review of Geophysics*, *32*(4), 363–403. <https://doi.org/10.1029/94RG01872>
- Laufkötter, C., John, J. G., Stock, C. A., & Dunne, J. P. (2017). Temperature and oxygen dependence of the remineralization of organic matter. *Global Biogeochemical Cycles*, *31*(7), 1038–1050. <https://doi.org/10.1002/2017GB005643>
- Lehette, P., & Hernández-León, S. (2009). Zooplankton biomass estimation from digitized images: A comparison between subtropical and Antarctic organisms. *Limnology and Oceanography: Methods*, *7*(4), 304–308. <https://doi.org/10.4319/lom.2009.7.304>
- Long, A. M., Jurgensen, S. K., Petchel, A. R., Savoie, E. R., & Brum, J. R. (2021). Microbial ecology of oxygen minimum zones amidst ocean deoxygenation. *Frontiers in Microbiology*, *3272*. <https://doi.org/10.3389/fmicb.2021.748961>
- Lovato, T., Peano, D., Butenschön, M., Materia, S., Iovino, D., Scoccimarro, E., et al. (2022). CMIP6 simulations with the CMCC Earth system model (CMCC-ESM2). *Journal of Advances in Modeling Earth Systems*, *14*(3), e2021MS002814. <https://doi.org/10.1029/2021MS002814>
- Lovecchio, E. (2025). [Dataset] ROMS+BEC coupled model output for the northern Benguela upwelling system. PANGAEA. <https://doi.org/10.1594/PANGAEA.967161>
- Lovecchio, E., Gruber, N., Münnich, M., & Lachkar, Z. (2017). On the long-range offshore transport of organic carbon from the Canary Upwelling System to the open North Atlantic. *Biogeosciences*, *14*(13), 3337–3369. <https://doi.org/10.5194/bg-14-3337-2017>
- Lovecchio, E., Henson, S., Carvalho, F., & Briggs, N. (2022). Oxygen variability in the offshore northern Benguela Upwelling System from glider data. *Journal of Geophysical Research: Oceans*, *127*(11), e2022JC019063. <https://doi.org/10.1029/2022JC019063>
- Lovecchio, E., Henson, S. A., Carvalho, F., & Briggs, N. (2023). NetCDF median glider data collected in the northern Benguela during February - June 2018. PANGAEA. [Dataset]. <https://doi.org/10.1594/PANGAEA.938221>
- Lovecchio, E., Henson, S. A., Carvalho, F., Briggs, N., & Hilder, H. (2025). NetCDF mean underwater glider data collected in the Northern Benguela during February - June 2018. Part 2: Optical backscattering and fluorescence data. PANGAEA. [Dataset]. <https://doi.org/10.1594/PANGAEA.967162>
- Ma, J., French, K. L., Cui, X., Bryant, D. A., & Summons, R. E. (2021). Carotenoid biomarkers in Namibian shelf sediments: Anoxygenic photosynthesis during sulfide eruptions in the Benguela Upwelling System. *Proceedings of the National Academy of Sciences*, *118*(29), e2106040118. <https://doi.org/10.1073/pnas.2106040118>
- Maas, A. E., Frazer, S. L., Outram, D. M., Seibel, B. A., & Wishner, K. F. (2014). Fine-scale vertical distribution of macroplankton and micronekton in the Eastern Tropical North Pacific in association with an oxygen minimum zone. *Journal of Plankton Research*, *36*(6), 1557–1575. <https://doi.org/10.1093/plankt/fbu077>
- Mackenzie, K. V. (1981). 9-term equation for sound speed in the oceans. *Journal of the Acoustical Society of America*, *70*(3), 807–812. <https://doi.org/10.1121/1.386920>
- Mahowald, N. M., Baker, A. R., Bergametti, G., Brooks, N., Duce, R. A., Jickells, T. D., et al. (2005). Atmospheric global dust cycle and iron inputs to the ocean. *Global Biogeochemical Cycles*, *19*(4), GB4025. <https://doi.org/10.1029/2004GB002402>
- Marlow, J. R., Farrimond, P., & Rosell-Melé, A. (2001). Analysis of lipid biomarkers in sediments from the Benguela Current coastal upwelling system (Site 1084). *Proceedings of the Ocean Drilling Program, Scientific Results*, *175*, 1–26. [http://www-odp.tamu.edu/PUBLICATIONS/175\\_SR/VOLUME/CHAPTERS/SR175\\_05.PDF](http://www-odp.tamu.edu/PUBLICATIONS/175_SR/VOLUME/CHAPTERS/SR175_05.PDF)
- Martin, J. H., Knauer, G. A., Karl, D. M., & Broenkow, W. W. (1987). Vertex: Carbon cycling in the northeast Pacific. *Deep-Sea Research, Part A: Oceanographic Research Papers*, *34*(2), 267–285. [https://doi.org/10.1016/0198-0149\(87\)90086-0](https://doi.org/10.1016/0198-0149(87)90086-0)
- Mayor, D. J., Gentleman, W. C., & Anderson, T. R. (2020). Ocean carbon sequestration: Particle fragmentation by copepods as a significant unrecognised factor? Explicitly representing the role of copepods in biogeochemical models may fundamentally improve understanding of future ocean carbon storage. *BioEssays*, *42*(12), 2000149. <https://doi.org/10.1002/bies.202000149>
- McDougall, T., & Barker, P. (2011). Getting started with teos-10 and the Gibbs seawater (GSW) oceanographic toolbox. 28pp., <http://www.teos-10.org> (Tech. Rep.). Retrieved from <http://www.teos-10.org>
- Modis AquaNASA Goddard Space Flight Center, Ocean Ecology Laboratory, Ocean Biology Processing Group. (2014). MODIS-aqua ocean color data; NASA Goddard space flight center, ocean ecology laboratory. *Ocean Biology Processing Group*. [Dataset]. [https://doi.org/10.5067/AQUA/MODIS\\_OC.2014.0](https://doi.org/10.5067/AQUA/MODIS_OC.2014.0)
- Mollenhauer, G., Inthorn, M., Vogt, T., Zabel, M., Sinninghe Damsté, J. S., & Eglinton, T. I. (2007). Aging of marine organic matter during cross-shelf lateral transport in the Benguela upwelling system revealed by compound-specific radiocarbon dating. *Geochemistry, Geophysics, Geosystems*, *8*(9), Q09004. <https://doi.org/10.1029/2007GC001603>

- Monteiro, P. M., Nelson, G., Van Der Plas, A., Mabilbe, E., Bailey, G. W., & Klingelhoeffer, E. (2005). Internal tide—Shelf topography interactions as a forcing factor governing the large-scale distribution and burial fluxes of particulate organic matter (POM) in the Benguela upwelling system. *Continental Shelf Research*, 25(15), 1864–1876. <https://doi.org/10.1016/j.csr.2005.06.012>
- Moore, J. K., Doney, S. C., & Lindsay, K. (2004). Upper ocean ecosystem dynamics and iron cycling in a global three-dimensional model. *Global Biogeochemical Cycles*, 18(4). <https://doi.org/10.1029/2004GB002220>
- Moore, J. K., Lindsay, K., Doney, S. C., Long, M. C., & Misumi, K. (2013). Marine ecosystem dynamics and biogeochemical cycling in the community Earth system model [CESM1(BGC)]: Comparison of the 1990s with the 2090s under the RCP4.5 and RCP8.5 scenarios. *Journal of Climate*, 26(23), 9291–9312. Retrieved Feb 13, 2023. <https://doi.org/10.1175/JCLI-D-12-00566.1>
- Morel, A., & Berthon, J.-F. (1989). Surface pigments, algal biomass profiles, and potential production of the euphotic layer: Relationships reinvestigated in view of remote-sensing applications. *Limnology & Oceanography*, 34(8), 1545–1562. <https://doi.org/10.4319/lo.1989.34.8.1545>
- Muller, A. A., Reason, C. J. C., Schmidt, M., Mohrholz, V., & Eggert, A. (2014). Computing transport budgets along the shelf and across the shelf edge in the northern Benguela during summer (DJF) and winter (JJA). *Journal of Marine Systems*, 140, 82–91. <https://doi.org/10.1016/j.jmarsys.2014.02.007>
- Naqvi, S. W. A. (1994). Denitrification processes in the Arabian Sea. *Proceedings of the Indian Academy of Sciences – Section A*, 103(2), 279–300. <https://doi.org/10.1007/BF02839539>
- Naqvi, S. W. A., Kumar, M. D., Narvekar, P. V., De Sousa, S. N., George, M. D., & D'Silva, C. (1993). An intermediate nepheloid layer associated with high microbial metabolic rates and denitrification in the northwest Indian Ocean. *Journal of Geophysical Research: Oceans*, 98(C9), 16469–16479. <https://doi.org/10.1029/93JC00973>
- NASA-OBPG SeaWiFS. (2014). NASA Goddard space flight center, ocean ecology laboratory, ocean biology processing group, sea-viewing wide field-of-view sensor. *SeaWiFS chlorophyll data*. [Dataset]. <https://doi.org/10.5067/ORBVIEW-2/SEAWIFS/L3M/CHL/2014>
- Oschlies, A., Brandt, P., Stramma, L., & Schmidtko, S. (2018). Drivers and mechanisms of ocean deoxygenation. *Nature Geoscience*, 11(7), 467–473. <https://doi.org/10.1038/s41561-018-0152-2>
- Pak, H., Codispoti, L. A., & Zaneveld, J. R. V. (1980). On the intermediate particle maxima associated with oxygen-poor water off western South America. *Deep-Sea Research, Part A: Oceanographic Research Papers*, 27(10), 783–797. [https://doi.org/10.1016/0198-0149\(80\)90044-8](https://doi.org/10.1016/0198-0149(80)90044-8)
- Palmiéri, J., Anderson, T., Yool, A., Martin, A., & Mayor, D. (2021). Introducing particle associated copepods in MEDUSA. <https://ukesm.ac.uk/portfolio-item/introducing-particle-associated-copepods-in-medusa/> (last accessed 10 august 2023)
- Rasse, R., & Dall'Olmo, G. (2019). Do oceanic hypoxic regions act as barriers for sinking particles? A case study in the eastern tropical North Atlantic. *Global Biogeochemical Cycles*, 33(12), 1611–1630. <https://doi.org/10.1029/2019GB006305>
- Rouffier, F., Berline, L., Guidi, L., Durrieu De Madron, X., Picheral, M., Sciandra, A., et al. (2014). Particle size distribution and estimated carbon flux across the Arabian Sea oxygen minimum zone. *Biogeosciences*, 11(16), 4541–4557. <https://doi.org/10.5194/bg-11-4541-2014>
- Sanders, R. J., Henson, S. A., Martin, A. P., Anderson, T. R., Bernardello, R., Enderlein, P., et al. (2016). Controls over ocean mesopelagic interior carbon storage (comics): Fieldwork, synthesis, and modeling efforts. *Frontiers in Marine Science*, 3, 136. <https://doi.org/10.3389/fmars.2016.00136>
- Schnetzer, A., & Steinberg, D. K. (2002). Active transport of particulate organic carbon and nitrogen by vertically migrating zooplankton in the Sargasso sea. *Marine Ecology Progress Series*, 234, 71–84. <https://doi.org/10.3354/meps234071>
- Séférian, R., Berthet, S., Yool, A., Palmiéri, J., Bopp, L., Tagliabue, A., et al. (2020). Tracking improvement in simulated marine biogeochemistry between CMIP5 and CMIP6. *Current Climate Change Reports*, 6(3), 95–119. <https://doi.org/10.1007/s40641-020-00160-0>
- Shchepetkin, A. F., & McWilliams, J. C. (2005). The regional oceanic modeling system (ROMS): A split-explicit, free-surface, topography-following-coordinate oceanic model. *Ocean Modelling*, 9(4), 347–404. ISSN 1463-5003. <https://doi.org/10.1016/j.ocemod.2004.08.002>
- Sherwood, C. R., Aretxabaleta, A. L., Harris, C. K., Rinehimer, J. P., Verney, R., & Ferré, B. (2018). Cohesive and mixed sediment in the regional ocean modeling system (ROMS v3.6) implemented in the coupled ocean–Atmosphere–Wave–Sediment transport modeling system (COAWST r1234). *Geoscientific Model Development*, 11(5), 1849–1871. <https://doi.org/10.5194/gmd-11-1849-2018>
- Siegfried, L., Schmidt, M., Mohrholz, V., Pogrzeba, H., Nardini, P., Böttinger, M., & Scheuermann, G. (2019). The tropical-subtropical coupling in the Southeast Atlantic from the perspective of the northern Benguela upwelling system. *PLoS One*, 14(1), e0210083. <https://doi.org/10.1371/journal.pone.0210083>
- Stuart, V., & Pillar, S. C. (1990). Diel grazing patterns of all ontogenetic stages of *Euphausia lucens* and in situ predation rates on copepods in the southern Benguela upwelling region. *Marine Ecology Progress Series*, 64(3), 227–241. <https://doi.org/10.3354/meps064227>
- Tarling, G. A., & Johnson, M. L. (2006). Satiation gives krill that sinking feeling. *Current Biology*, 16(3), R83–R84. <https://doi.org/10.1016/j.cub.2006.01.044>
- Ulloa, O., Canfield, D. E., DeLong, E. F., Letelier, R. M., & Stewart, F. J. (2012). Microbial oceanography of anoxic oxygen minimum zones. *Proceedings of the National Academy of Sciences*, 109(40), 15996–16003. <https://doi.org/10.1073/pnas.1205009109>
- Vaquer-Sunyer, R., & Duarte, C. M. (2008). Thresholds of hypoxia for marine biodiversity. *Proceedings of the National Academy of Sciences*, 105(40), 15452–15457. <https://doi.org/10.1073/pnas.0803833105>
- Volkman, J. K. (2006). Lipid biomarkers for marine organic matter. *Marine Organic Matter: Biomarkers, Isotopes and DNA The Handbook of Environmental Chemistry*, 2, 27–70. ISSN 1867-979X.
- Wainright, S. C., & Hopkinson Jr, C. S. (1997). Effects of sediment resuspension on organic matter processing in coastal environments: A simulation model. *Journal of Marine Systems*, 11(3–4), 353–368. [https://doi.org/10.1016/S0924-7963\(96\)00130-3](https://doi.org/10.1016/S0924-7963(96)00130-3)
- Waite, A. M., Stemann, L., Guidi, L., Calil, P. H. R., Hogg, A. M. C., Feng, M., et al. (2016). The wineglass effect shapes particle export to the deep ocean in mesoscale eddies. *Geophysical Research Letters*, 43(18), 9791–9800. <https://doi.org/10.1002/2015GL066463>
- Wakeham, S. G. (1995). Lipid biomarkers for heterotrophic alteration of suspended particulate organic matter in oxygenated and anoxic water columns of the ocean. *Deep-Sea Research Part I*, 42(10), 1749–1771. [https://doi.org/10.1016/0967-0637\(95\)00074-G](https://doi.org/10.1016/0967-0637(95)00074-G)
- Ward, B. B., Tuit, C. B., Jayakumar, A., Rich, J. J., Moffett, J., & Naqvi, S. W. A. (2008). Organic carbon, and not copper, controls denitrification in oxygen minimum zones of the ocean. *Deep Sea Research Part I: Oceanographic Research Papers*, 55(12), 1672–1683. <https://doi.org/10.1016/j.dsr.2008.07.005>
- Ward, P., Atkinson, A., & Tarling, G. (2012). Mesozooplankton community structure and variability in the Scotia sea: A seasonal comparison. *Deep Sea Research Part II: Topical Studies in Oceanography*, 59, 78–92. <https://doi.org/10.1016/j.dsr2.2011.07.004>
- Werner, T., & Buchholz, F. (2013). Diel vertical migration behaviour in euphausiids of the northern Benguela current: Seasonal adaptations to food availability and strong gradients of temperature and oxygen. *Journal of Plankton Research*, 35(4), 792–812. <https://doi.org/10.1093/plankt/fbt030>
- Whitmire, A. L., Letelier, R. M., Villagrán, V., & Ulloa, O. (2009). Autonomous observations of in vivo fluorescence and particle backscattering in an oceanic oxygen minimum zone. *Optics Express*, 17(24), 21992–22004. <https://doi.org/10.1364/OE.17.021992>

- Wishner, K. F., Ashjian, C. J., Gelfman, C., Gowing, M. M., Kann, L., Levin, L. A., et al. (1995). Pelagic and benthic ecology of the lower interface of the Eastern Tropical Pacific oxygen minimum zone. *Deep Sea Research Part I: Oceanographic Research Papers*, *42*(1), 93–115. [https://doi.org/10.1016/0967-0637\(94\)00021-J](https://doi.org/10.1016/0967-0637(94)00021-J)
- Wishner, K. F., Outram, D. M., Seibel, B. A., Daly, K. L., & Williams, R. L. (2013). Zooplankton in the eastern tropical north Pacific: Boundary effects of oxygen minimum zone expansion. *Deep Sea Research Part I: Oceanographic Research Papers*, *79*, 122–140. ISSN 0967-0637. <https://doi.org/10.1016/j.dsr.2013.05.012>
- WOA2018 Oxygen [Dataset]. Statistical mean of dissolved oxygen on 1° grid for all decades, Retrieved from <https://www.ncei.noaa.gov/access/world-ocean-atlas-2018/bin/woa18oxnu.pl> (last accessed: 14 August 2023) .
- WOA2023 Salinity [Dataset]. Statistical mean of salinity on 1° grid for 1991–2020 years, Retrieved from <https://www.ncei.noaa.gov/access/world-ocean-atlas-2023/bin/woa23.pl> (last accessed: 14 August 2023) .
- Wojtasiewicz, B., Trull, T. W., Udaya Bhaskar, T. V. S., Gauns, M., Prakash, S., Ravichandran, M., et al. (2020). Autonomous profiling float observations reveal the dynamics of deep biomass distributions in the denitrifying oxygen minimum zone of the Arabian Sea. *Journal of Marine Systems*, *207*, 103103. 0924-7963. <https://doi.org/10.1016/j.jmarsys.2018.07.002>
- Yang, S., Gruber, N., Long, M. C., & Vogt, M. (2017). ENSO driven variability of denitrification and suboxia in the Eastern Tropical Pacific Ocean. *Global Biogeochemical Cycles*, *31*(10), 1470–1487. <https://doi.org/10.1002/2016GB005596>

## References From the Supporting Information

- Colella, P., & Woodward, P. R. (1984). The piecewise parabolic method (PPM) for gas-dynamical simulations. *Journal of Computational Physics*, *54*(1), 174–201. ISSN 0021-9991. [https://doi.org/10.1016/0021-9991\(84\)90143-8](https://doi.org/10.1016/0021-9991(84)90143-8)
- Donlon, C. J., Martin, M., Stark, J. D., Roberts-Jones, J., Fiedler, E., & Wimmer, W. (2011). The operational sea surface temperature and sea ice analysis (OSTIA). *Remote Sensing of Environment*, *116*, 140–158. <https://doi.org/10.1016/j.rse.2010.10.017>
- Lauvset, S. K., Key, R. M., Olsen, A., van Heuven, S., Velo, A., Lin, X., et al. (2016). A new global interior ocean mapped climatology: The 1° × 1° GLODAP version 2. *Earth System Science Data*, *8*, 325–340. <https://doi.org/10.5194/essd-8-325-2016>
- Löscher, C. R., Bange, H. W., Schmitz, R. A., Callbeck, C. M., Engel, A., Hauss, H., et al. (2016). Water column biogeochemistry of oxygen minimum zones in the eastern tropical North Atlantic and eastern tropical South Pacific oceans. *Biogeosciences*, *13*(12), 3585–3606. <https://doi.org/10.5194/bg-13-3585-2016>
- Rio, M. H., Mulet, S., & Picot, N. (2014). Beyond GOCE for the ocean circulation estimate: Synergetic use of altimetry, gravimetry, and in situ data provides new insight into geostrophic and Ekman currents. *Geophysical Research Letters*, *41*(24), 8918–8925. <https://doi.org/10.1002/2014GL061773>